Structures 56 (2023) 104715

Contents lists available at ScienceDirect

Structures

journal homepage: www.elsevier.com/locate/structures

Nonlinear computational framework for hybrid ductile glulam joists

Chenyang Cao, Wendel Sebastian *

Department of Civil, Environmental and Geomatic Engineering, University College London, Chadwick Building, Gower Street, London WC1E 6BT, UK

ARTICLE INFO

Keywords:
Nonlinear analysis
Glulam
Hybrid joists
Ductility
Section constitutive behaviors
Longitudinal shear stress

ABSTRACT

This paper starts by presenting a nonlinear algebraic analysis of hybrid glulam sections, including ductile compression-softening constitutive models obtained via regression analysis of material test data, to compute full-range admissible values of moment (M), co-existent curvature (κ) and excluded-area axial force (F_{ea}) for the sections. The (M, κ, F_{ea}) states, double-checked by treating the section alternately as discretised and as a continuum, are clustered into (M, κ) and (M, F_{ea}) data-sets that permit regression-analysis of κ and F_{ea} as polynomial functions of M. For any load on a glulam member the M profile is known, so $\kappa(M)$ is a more efficient route to calculating deflections than is $M(\kappa)$. The $\kappa(M)$ and $F_{ea}(M)$ constitutive functions, which enable assessment of any section state without tedious recalculation, are fused with longitudinal compatibility and equilibrium requirements to predict the joists' nonlinear responses up to ultimate. Using quartic or Glos compressive constitutive models, spreadsheet-coding of this framework is shown to predict nonlinear local ($\kappa(M)$) and global (load–deflection) responses close to test data, also axial and longitudinal-shear stress redistributions mimicking FE predictions for distributed- or point-loaded hybrid glulam joists comprising combinations of poplar, blue-gum, maritime-pine and larch. The results show that post-peak reductions on compressive stress–strain curves cause through-depth reversal of longitudinal-shear at high moments.

1. Introduction

Timber has a long history as a construction material. The industrial revolution saw uses of timber and stone drop in favour of concrete and steel, but there is now a resurgence of interest in timber for inspired applications in flexural and axial-flexural members [1,2]. This is owing to timber's excellent specific mechanical properties, low-carbon credentials, availability of machinery for processing it into engineered members with good quality control on material properties, and the ease with which it is prefabricated into modules [2].

In these applications, a notable influencing factor on the load response is timber's asymmetric constitutive behaviour between tension and compression along the grain. Under tensile stress timber is linear up to brittle fracture, while in compression the material exhibits distinct softening behaviour that gives rise to a nonlinear stress–strain characteristic which approximates ductility in the approach to failure. This change of constitutive behaviour with stress reversal (albeit along a given line) may be viewed as another manifestation of anisotropy in timber. The nonlinear compressive behaviour is insignificant for flexural applications where the timber is overall a tension bottom chord, e.g. in timber-concrete composites under positive moments [3–6]). However, it can be pronounced in applications where the timber is a compression top chord as in steel-timber composites under positive moments [7], or a compression bottom chord as in timber-concrete composites under negative moments [8], or indeed where longitudinal timber joists act non-compositely e.g. in timber bridges with decks comprising transverse timber slats [9], or also as timber columns [10].

Multiple models have been used to describe the nonlinear compressive strain–stress behaviour of timber in the parallel-to-grain direction. The bilinear model is often used, comprising an ascending segment up to a peak stress, followed by a linear falling segment [11–14]. As an alternative, Lam et al. [15] used a cubic polynomial function for the compressive behaviour up to peak stress, thus giving a sectioned polynomial model for the strain–stress relationship. Glos et al. developed a constitutive model describing the compressive curve which gives a good approximation up to failure [16,17]. Further, different three-dimensional constitutive models for timber have been developed to describe the elasto-plastic nature of the material [18–20].

These parallel-to-grain constitutive behaviours mean that, if designed properly, a timber joist in flexure under load can be made to exhibit significant ductility by activating nonlinear behaviour in the peak compression zone before brittle failure occurs in the peak tension

* Corresponding author.
E-mail address: W.Sebastian@ucl.ac.uk (W. Sebastian).

https://doi.org/10.1016/j.istruc.2023.06.046
Received 15 March 2023; Received in revised form 29 May 2023; Accepted 9 June 2023
Available online 10 August 2023

zone. Hybrid joists show strong potential to achieve such ductile failures because they can be optimised to combine modest strength ductile material in the compression zone with high strength material in the tension zone. In other words, the hybrid glulam joists use lamellae of different strength classes arranged in stacking sequences that promote softening of the extreme compression zone at advanced stages of flexure. The joist's overall failure behaviour is thus dominated by nonlinear compression ductility before fracture occurs in the tension zone. Another approach to enhance ductility is the use of steel reinforcement designed to yield before the timber fails in flexure.

In both cases the ductility is manifest either at the local section level via the moment- curvature plots, or at the global member level via the load–deflection plots. Using flexural tests, Martins [21] showed member level ductility for maritime pine-poplar and blue gum-poplar hybrid joists, while Tomasi et al. [23] showed section level ductility for poplar-larch and poplar-spruce hybrids.

Alongside testing, it is important to have a nonlinear analysis tool for predicting member response particularly in the approach to failure, when stresses and deflections show increasing rates of change with load. Prediction of deflections is important given the low moduli of timbers and the need to understand global ductility characteristics, while prediction of flexural and longitudinal shear stress redistributions is crucial to understanding failure modes.

It is desirable to build these nonlinear predictive capabilities into an interactive, universally accessible application such as a spreadsheet that is rigorously based on structural mechanics. To that end, Shioya [22] used algebraic analysis to explore timber-steel hybrids. The present paper strongly advances these above previous studies by presenting a computational framework, founded on two section constitutive characteristics (SCCs) each defined by a high-order polynomial equation, for nonlinear structural analysis of hybrid glulam members. The SCCs emerge from data sets defining co-existent values of curvature (κ), moment (M) and excluded area axial force (F_{ea}) which mathematically define the nonlinearly evolving section states from the unloaded condition to failure. In order to define each admissible (M, κ, F_{ea}) state, section compatibility requirements based on relaxing shear deformations are combined with experimentally-based tensile and compressive material constitutive behaviours, subject to the equilibrium requirement for zero net axial force on the section.

Once the moment diagram is established for any given load, the SCCs enable rapid and full determination of the corresponding section states along a glulam member, throughout the nonlinear regime. This avoids tedious recalculation of section states from scratch, which renders this approach both computationally-efficient and time saving.

This twin-SCC based computational framework embeds three novelties, namely:

(1) It double-checks the (M,κ,F_{ea}) states which underpin the SCCs, by treating the section alternately as discretised into thin layers (the individual axial force and moment contributions of which are summed) and as a continuum (for which integration is used as the summation tool).
(2) It reverses the traditional $M(\kappa)$ approach by using $\kappa(M)$ as one of the section constitutive characteristics. That is to say, curvature is expressed as a polynomial function of moment by conducting regression analysis of the derived (M, κ) data set. This chimes with the fact that M is naturally the independent variable with respect to κ, since the moment diagram is readily obtained for any given applied load. Hence, based on the moment diagram, $\kappa(M)$ has the advantage of enabling ready determination of the curvature profile along the span, which in turn hugely facilitates determination of the deflection profile at any stage of nonlinearity. Moreover, the continuity of the $\kappa(M)$ polynomial function avoids the need, for intermediate values of M, to interpolate between the original points.
(3) This study further introduces a $F_{ea}(M)$ constitutive characteristic which, when combined with longitudinal equilibrium considerations, as illustrated later, permits prediction of longitudinal shear-bond stresses at any stage of nonlinearity. These stresses are important at the adhesively-bonded interfaces between lamellae and within the timber parallel to the grain where the shear stress capacity can be limited.

This computational framework is powerful, because (as shown later) it quantifies local and global ductile behaviours, along with nonlinear stress redistributions in good agreement with tests (displacements only) and FE analysis (both displacements and stresses). Also, very importantly, there is a universality about the framework, because it is eminently suited to implementation in a spreadsheet. Hence it can be implemented in design offices (where nonlinear analysis capabilities are often limited) as well as in research environments.

In what follows the fundamentals and spreadsheet implementation of the framework are presented. Then, results from its use are compared with test and FE outputs for the two experimental programmes described earlier, namely one by Martins [21] and the other by Tomasi et al. [23]. Finally, in closing, potential wider applications of this computational framework are discussed.

Note that the commercial software program ABAQUS has been used to generate the FE results. To that end it must be emphasised that the experimental data permit validation of the present computational framework's predicted load–deflection behaviour, but not of its predicted shear stresses. It is the Abaqus finite element modelling (itself verified via the test load–deflection data) which permits validation of

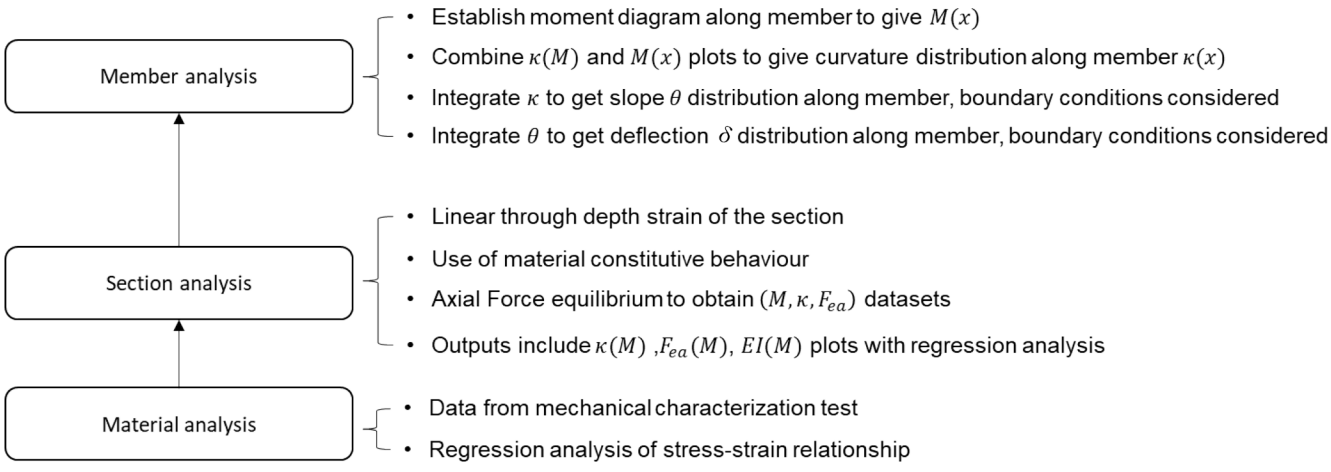

Fig. 1. Flow chart of the computational framework.

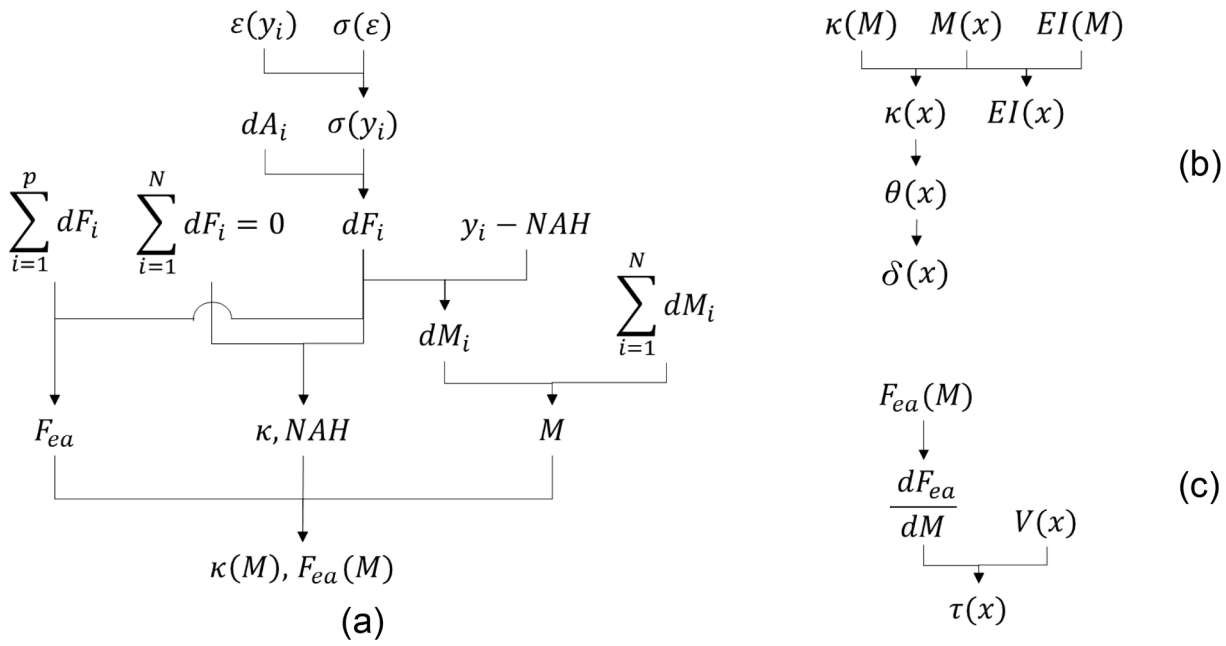

Fig. 2. Modelling Strategy (a) Section Constitutive behaviour (b) Member deflection (c) Longitudinal shear bond stress.

Table 1
Comparison between using one decimal place and six decimal places at ultimate for section H3 (defined later).

	Neutral Axis Height (mm)	Section Bending Moment (*kNM*)
Six decimal coefficients	45.45	20.50
One decimal coefficient	45.54	22.88
Percentage Difference	0.2%	11.6%

the flexural and shear stress predictions from the computational method.

2. Computational modelling strategy

2.1. General description

The computational modelling strategy for ductile hybrid glulam joists is founded on the hierarchical approach shown in Fig. 1, whereby the material level constitutive behaviour feeds into the section level and finally the overall member level constitutive behaviours. The approach utilises high order polynomial curve fits (obtained by regression analysis) to mathematically define the materials' experimentally obtained constitutive behaviours. After so-defining material behaviour, the approach moves on to define the hybrid sections' constitutive behaviours by combining the resulting material nonlinear stress–strain behaviour with compatibility (namely linear through-depth distribution of flexural strains with zero shear deformation) and equilibrium of stress resultants. Fig. 2 outlines this methodology based on discretisation of the section into N thin layers. In order to check the validity of this approach, an alternative (described in Section 2.3) based on treating the section as a continuum was also used.

It was observed that the overall accuracy of the computations is influenced by the fidelity (number of decimal places) of the polynomial coefficients particularly of the higher order terms. As an example, for the sections used by Martins [21], Table 1 shows the differences obtained (using the present approach) in section neutral axis heights (*NAH* s) and

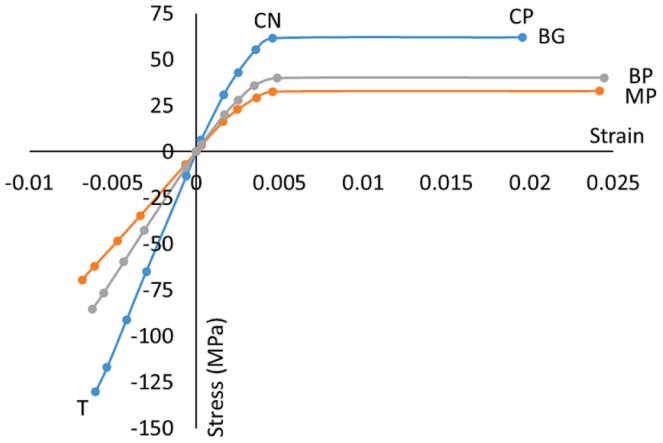

Fig. 3. Material constitutive behaviour from study by Martins [21].

bending moments, when one decimal place was used instead of six for the material constitutive coefficients. It is seen that while the *NAH* was virtually unaffected, the section moment exhibits an 11.6% increase due to the change in decimal places. Now 1.116 can be comparable to some safety factors used in structural design codes, so an 11.6% error may be considered on the limit of acceptability. Thus, to eliminate the error, the coefficients in the polynomial equations were used to several significant figures.

Another important issue in this study is adequate representation of the nonlinear flexural stiffness variation along the span, especially in the zones of maximum and varying moment. To that end note, in the first two lines of Fig. 2(b), use of the section flexural stiffness profile to inform the distribution of calculation sections along the span, with zones of rapidly changing stiffness prompting more closely spaced sections. This point will be picked up again later in this paper during the verification study.

It is worth recalling the notable feature of this approach that the full range of each relevant section constitutive characteristic (namely the $\kappa(M)$, $F_{ea}(M)$ and indeed the $EI(M)$ constitutive curves from the unloaded

Table 2
Regression equations for timber species used in study by Martins [21].

‘	Stage	Regression Equation	ε Range
BG	Tension	$\sigma = 21666.748962\varepsilon$ $(R^2 = 0.999874)$	−0.00603–0
	Compression Nonlinear	$\sigma = -77259308571.5\varepsilon^4 + 647392495.136719\varepsilon^3 - 3416932.682854\varepsilon^2 + 22928.677606\varepsilon$ $(R^2 = 0.999999)$	0–0.00456
	Compression plateau	$\sigma = 0.333778\varepsilon + 61.347797$ $(R^2 = 1)$	0.00456–0.01945
BP	Tension	$\sigma = 10179.946638\varepsilon$ $(R^2 = 0.999895)$	−0.00683–0
	Compression Nonlinear	$\sigma = -2206134657.75\varepsilon^4 + 11051617.880859\varepsilon^3 - 1006350.775227\varepsilon^2 + 11785.587267\varepsilon$ $(R^2 = 0.999969)$	0–0.00456
	Compression plateau	$\sigma = 0.152905\varepsilon + 32.630275$ $(R^2 = 1)$	0.00456–0.02418
MP	Tension	$\sigma = 13774.444609\varepsilon$ $(R^2 = 0.999975)$	−0.00621–0
	Compression Nonlinear	$\sigma = -62510163835.625\varepsilon^4 + 434624728.515625\varepsilon^3 - 1845411.974476\varepsilon^2 + 14063.318406\varepsilon$ $(R^2 = 0.999995)$	0–0.00483
	Compression near plateau	$\sigma = 0.101937\varepsilon + 39.750765$ $(R^2 = 1)$	0.00483–0.02445

section up to failure) is determined only once, including definition of a polynomial equation via regression analysis of the data points, this equation then being repeatedly used in tandem with any admissible values of moment and shear force derived from global equilibrium along the joist. This means that the relevant section response does not have to be re-calculated from scratch for admissible moment values in-between those corresponding to the original points on the characteristics. This feature makes the present computational strategy both computationally efficient and time-economic.

2.2. Material constitutive behaviour

The parallel-to-grain uni-axial stress–strain relationship for each timber species is presented as a high-order polynomial equation obtained by regression analysis (curve fits) of the available material test data. For the two verification examples considered later in this paper, four species of timber, namely Maritime Pine (MP), Blue Gum (BG), Poplar (BP) and larch were used. Multiple coupon tests were conducted in one study by Martins [21] on three of the timber species, and in the other independent study by Tomasi et al [23] on two of the species, to check consistency and to limit errors within the test data. Fig. 3, which presents both the original test data points and the curve-fits for the study by Martins, shows that each species exhibits linear behaviour up to fracture under tensile stress, while in compression the relationship is initially linear with the same slope as the tension side, but then is followed at higher strains by a nonlinear regime and finally becomes a near-plateau in the close approach to failure.

For the study by Martins, a quartic equation has been adopted to describe the compressive stress–strain behaviour before the plateau as a nonlinear function of strain. On Fig. 3 T, CN and CP indicate the conclusions of the tension, compression nonlinear and compression plateau stages. The linear compression stage occurs only at low strains and the exact range is difficult to identify, so it is incorporated within the nonlinear function rather than being presented as a linear equation. The first derivative (tangent elastic modulus) of the quartic equation at the origin is similar to the slope of the tension linear equation as reflected by the equivalent left and right slopes at the origin in Fig. 3. That is to say, the tension and compression elastic moduli at zero strain are very

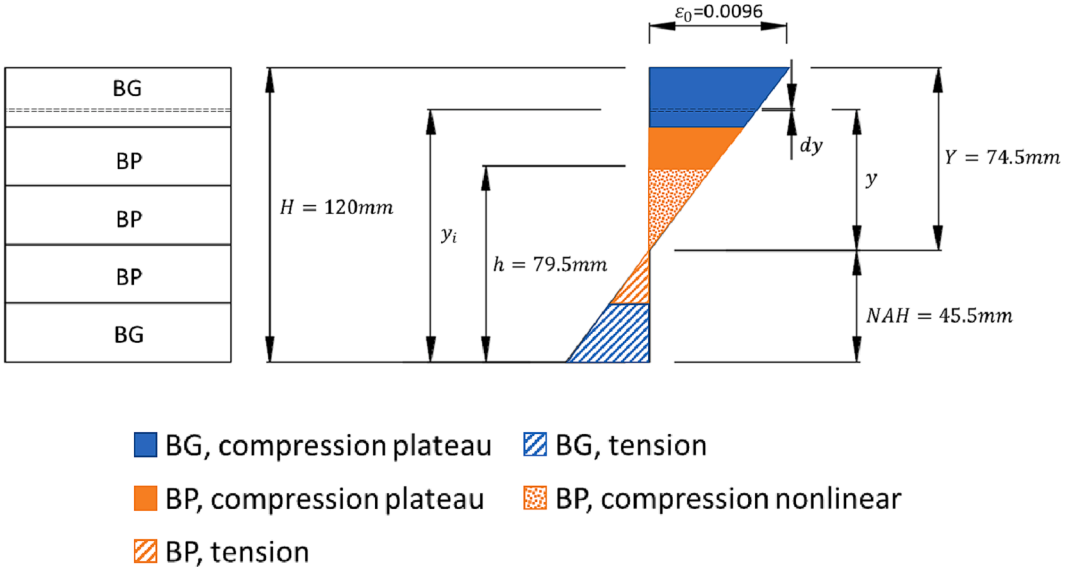

Fig. 4. Section H3 (from Martins [21]) at advanced compression nonlinearity.

similar to each other. These material constitutive equations, used later in the verification study based on the work by Martins [21], are summarised in Table 2. For the second verification study based on the work by Tomasi et al, a Glos model [16,17] was used for compression behaviour, as explained later.

2.3. Section constitutive behaviour

It is assumed that the through-depth distribution of flexural strain is linear, with zero slip between lamellas. The starting point for the section computations is the assumption of a material admissible strain (ε_0) at top of the section along with an assumed value for the associated neutral axis height *NAH*. That is to say, the section analysis starts by presupposing ε_0 to provide the initial strain condition, then a value of *NAH* is also guessed to enable the analysis to proceed. As shown in Fig. 4, in one approach the cross section is divided into *N* thin layers of the same thickness. The strain at mid-thickness of layer *i* is obtained as Equation (1) where y_i indicates the height of layer *i* and *H* refers to the height of the joist section.

$$\varepsilon(y_i) = \varepsilon_0 \frac{y_i - NAH}{H - NAH} \tag{1}$$

The bending stress at layer *i* is then derived by applying the material constitutive equation $\sigma(\varepsilon)$ to the given strain value $\varepsilon(y_i)$, then the corresponding axial force dF_i on layer *i* is determined as the product of the layer stress $\sigma(y_i)$ and the layer's cross sectional area dA_i. Axial force equilibrium of the entire section is achieved when the summation of dF_i across all layers equals to zero, as shown in Fig. 2(a).

In one approach, the above framework is used to compute the axial forces for all layers of the hybrid timber section. The sum of these layer forces may then be obtained as a function of the guessed *NAH* value. By coding the computations into an Excel spreadsheet, the "Goal Seek" function is used to iterate towards the *NAH* value which, for the given ε_0 value, enables the condition of zero net axial force on the section to be met. By successively incrementing the value of ε_0 and by finding the associated admissible *NAH* value as above, multiple section states from unloaded up to failure may be mathematically defined.

In the alternative approach, which is used to double-check the results from the layered approach, the compatibility (linear through-depth strain), material constitutive and axial force equilibrium requirements are combined using elemental calculus and integration, so as to emerge from the section analysis with a high order polynomial equation in *NAH* as the unknown. For the hybrid section H3 from Martins [21], used in the verification study presented later, the right hand side of Fig. 4 shows the key quantities required to produce this overall section high order polynomial equation for an advanced stage of nonlinearity. To that end Fig. 4 indicates the section layout, the through-depth strain distribution and the corresponding constitutive regimes (i.e. where the materials are along the stress–strain curves) for a state of pronounced compression softening in the upper reaches of the section.

Expression of the constitutive equations in terms of ε_0 and *y*, for the materials at different stages of behaviour through the section depth, can be found in Table 3.

Expression of the section's zero axial force equilibrium requirement via a highly nonlinear equation in *NAH* as derived using the calculus approach, is exemplified in Equations (2) and (3). Note that the axial force from each constitutive zone identified in Fig. 4 is calculated as the product of the width of the section (92 mm) and the summation of the stress × elemental area within each zone summarized in Table 3.

$$F_{BP,comp} + F_{BG,comp} + F_{BP,tens} + F_{BG,tens} = 0 \tag{2}$$

$$92\int_0^{h-NAH}\left[-2206134657.75\left(\frac{\varepsilon_0}{Y}y\right)^4 + 11051617.880859\left(\frac{\varepsilon_0}{Y}y\right)^3 - 1006350.775227\left(\frac{\varepsilon_0}{Y}y\right)^2 + 11785.587267\left(\frac{\varepsilon_0}{Y}y\right)\right]dy + 92\int_{h-NAH}^{96-NAH}\left[0.152905\left(\frac{\varepsilon_0}{Y}y\right) + 32.630275\right]dy + 92\int_{96-NAH}^{120-NAH}\left[0.333778\left(\frac{\varepsilon_0}{Y}y\right) + 61.347797\right]dy + 92\int_0^{24-NAH}\left[10179.946638\left(\frac{\varepsilon_0}{Y}y\right)\right]dy + 92\int_{24-NAH}^{-NAH}\left[21666.748962\left(\frac{\varepsilon_0}{Y}y\right)\right]dy = 0 \tag{3}$$

Using either the layer-based summation approach or this overall section polynomial equation approach, the "Goal Seek" function in Excel can be used to iterate through the computations until the admissible value of *NAH* is found by two independent means. Recalling that (ε_0) is automatically within the top layer material's compressive limit, it is also necessary to check whether the strain (ε_{bot}) at the base of the section exceeds the base material's limit in tension, i.e. whether material failure has occurred. If it has not, then the section curvature κ is obtained as Equation (4), namely:

$$\kappa = \varepsilon_{bot}/NAH \tag{4}$$

Note that in the layer-based approach, the bending moment contribution (dM_i) from each layer is obtained as the product of the element force (dF_i) in that layer and the lever arm (y_i - *NAH*) between the neutral axis and that layer, see Fig. 2(a). The section moment is then calculated as the summed contribution from all layers. Alternatively, in the continuum approach, the section's moment equation is obtained by integrating the calculus moment expression for an elemental strip, as presented in Equation (5) for the section and state assumed in Equation (3).

$$M = 92\int_0^{h-NAH}\left[-2206134657.75\left(\frac{\varepsilon_0}{Y}y\right)^4 + 11051617.880859\left(\frac{\varepsilon_0}{Y}y\right)^3 - 1006350.775227\left(\frac{\varepsilon_0}{Y}y\right)^2 + 11785.587267\left(\frac{\varepsilon_0}{Y}y\right)\right]ydy + 92 \times \int_{h-NAH}^{96-NAH}\left[0.152905\left(\frac{\varepsilon_0}{Y}y\right) + 32.630275\right]ydy + 92\int_{96-NAH}^{120-NAH}\left[0.333778\left(\frac{\varepsilon_0}{Y}y\right) + 61.347797\right]ydy + 92\int_0^{24-NAH}\left[10179.946638\left(\frac{\varepsilon_0}{Y}y\right)\right]ydy + 92 \times \int_{24-NAH}^{-NAH}\left[21666.748962\left(\frac{\varepsilon_0}{Y}y\right)\right]ydy \tag{5}$$

Table 3
Stress as a function of y.

Species (regime)	Regression Equation
BP (nonlinear)	$\sigma = -2206134657.75(\frac{\varepsilon_0}{Y}y)^4 + 11051617.880859(\frac{\varepsilon_0}{Y}y)^3 - 1006350.775227(\frac{\varepsilon_0}{Y}y)^2 + 11785.587267(\frac{\varepsilon_0}{Y}y)$
BP (plateau)	$\sigma = 0.152905(\frac{\varepsilon_0}{Y}y) + 32.630275$
BG (plateau)	$\sigma = 0.333778\left(\frac{\varepsilon_0}{Y}y\right) + 61.347797$
BP (tension)	$\sigma = 10179.946638\left(\frac{\varepsilon_0}{Y}y\right)$
BG (tension)	$\sigma = 21666.748962\left(\frac{\varepsilon_0}{Y}y\right)$

	A	B	C	D	E	F	G	H	I	J	K
1	BG					Material	h (mm)	ε	σ(Mpa)	F (N)	M (kN·m)
2	Max stress in tension			130		BG	120	0.008	61.35047	5644.243	0.400894
3	Strain			0.00603		BG	119	0.007888	61.35043	5644.24	0.395249
4	Max stress in compression			33		BG	118	0.007776	61.35039	5644.236	0.389605
5	90% strain			0.01954		BG	117	0.007664	61.35036	5644.233	0.38396
6	yield strain in compression			0.00456		BG	116	0.007553	61.35032	5644.229	0.378316
7	MP					BG	115	0.007441	61.35028	5644.226	0.372672
8	Max stress in tension			69.5		BG	114	0.007329	61.35024	5644.222	0.367027
9	Strain			0.00683		BG	113	0.007217	61.35021	5644.219	0.361383
10	Max stress in compression			32.7		BG	112	0.007105	61.35017	5644.216	0.355738
11	90% strain			0.02418		BG	111	0.006993	61.35013	5644.212	0.350094
12	yield strain in compression			0.00456		BG	110	0.006882	61.35009	5644.209	0.344449
13	Section layout					BG	109	0.00677	61.35006	5644.205	0.338805
14	Width	92	Height	120		BG	108	0.006658	61.35002	5644.202	0.333161
15	Layer	Material	Thickness	Height		BG	107	0.006546	61.34998	5644.198	0.327516
16	1	MP	24	120		BG	106	0.006434	61.34994	5644.195	0.321872
17	2	BP	24	96		BG	105	0.006322	61.34991	5644.191	0.316227
18	3	BP	24	72		BG	104	0.00621	61.34987	5644.188	0.310583
19	4	BP	24	48		BG	103	0.006099	61.34983	5644.185	0.304939
20	5	MP	24	24		BG	102	0.005987	61.3498	5644.181	0.299294
21	Section behaviour					BG	101	0.005875	61.34976	5644.178	0.29365
22	εtop	NAH	Sum F(N)			BG	100	0.005763	61.34972	5644.174	0.288005
23	0.008	48.47296	1.21867E-07			BG	99	0.005651	61.34968	5644.171	0.282361
24	εbottom	κ	Sum M (kN*M)			BG	98	0.005539	61.34965	5644.167	0.276717
25	0.005421	0.000112	19.14683343			BG	97	0.005428	61.34961	5644.164	0.271072
26						BG	96	0.005316	61.34957	5644.161	0.265428
27						BP	95	0.005204	32.63107	3002.059	0.138176
28						BP	94	0.005092	32.63105	3002.057	0.135174
29						BP	93	0.00498	32.63104	3002.055	0.132172
30						BP	92	0.004868	32.63102	3002.054	0.129169
31						BP	91	0.004756	32.631	3002.052	0.126167
32						BP	90	0.004645	32.63099	3002.051	0.123165
33						BP	89	0.004533	32.79142	3016.811	0.120754
34						BP	88	0.004421	32.4953	2989.567	0.116674
35						BP	87	0.004309	32.17119	2959.749	0.11255
36						BP	86	0.004197	31.81932	2927.378	0.108392
37						BP	85	0.004085	31.43993	2892.473	0.104207
38						BP	84	0.003974	31.03322	2855.056	0.100004
39						BP	83	0.003862	30.59939	2815.144	0.095791
40						BP	82	0.00375	30.13866	2772.756	0.091576
41						BP	81	0.003638	29.6512	2727.91	0.087367

... | 0.0035 | 0.004 | 0.0045 | 0.005 | 0.0055 | 0.006 | 0.0065 ...

Fig. 5. Spreadsheet layout for the layered approach.

Fig. 5 gives an example of the spreadsheet layout for the layered approach at a highly nonlinear stage for section H3.

The above analysis procedure is repeated with a gradually increasing top strain ε_0 at each new step. The curvature κ and associated bending moment M output from each such cluster of computations are recorded. Collectively, the (M,κ) points define section constitutive behaviour for curvature as a function of moment $\kappa(M)$ from zero curvature until section failure when either the top or the bottom strain reaches the material ultimate strain in compression or tension respectively. Note that the moment M is taken as the independent variable in $\kappa(M)$, so as to link the section constitutive behaviour to the along-joist equilibrium behaviour as shown shortly.

2.4. Member (joist) deflection profile

For known load and boundary conditions, the curvature distribution along the joist is determined by combining the section constitutive behaviour $\kappa(M)$ with the moment profile $M(x)$ at multiple locations along the span, where x is the distance along the beam from a suitable reference. Then, regression analysis (curve-fitting) of the (κ,x) points leads to a polynomial equation expressing curvature as a function of span location. This defines $\kappa(x)$, which is then successively integrated (including boundary conditions) to give the rotation $\theta(x)$ and deflection $\delta(x)$ profiles. Hence in addition to its use for defining the constitutive characteristics, the curve-fitting process is also valuable for addressing longitudinal compatibility relationships. Shear deflections are neglected

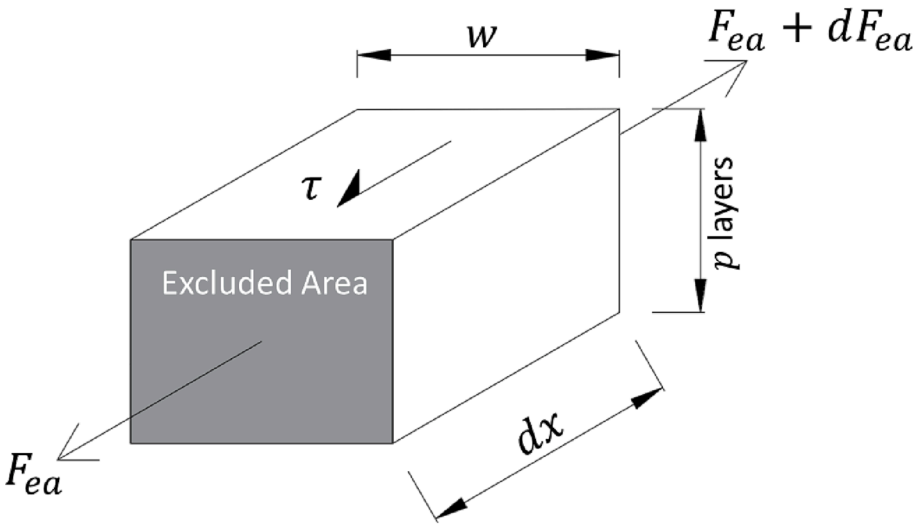

Fig. 6. Short portion equilibrium.

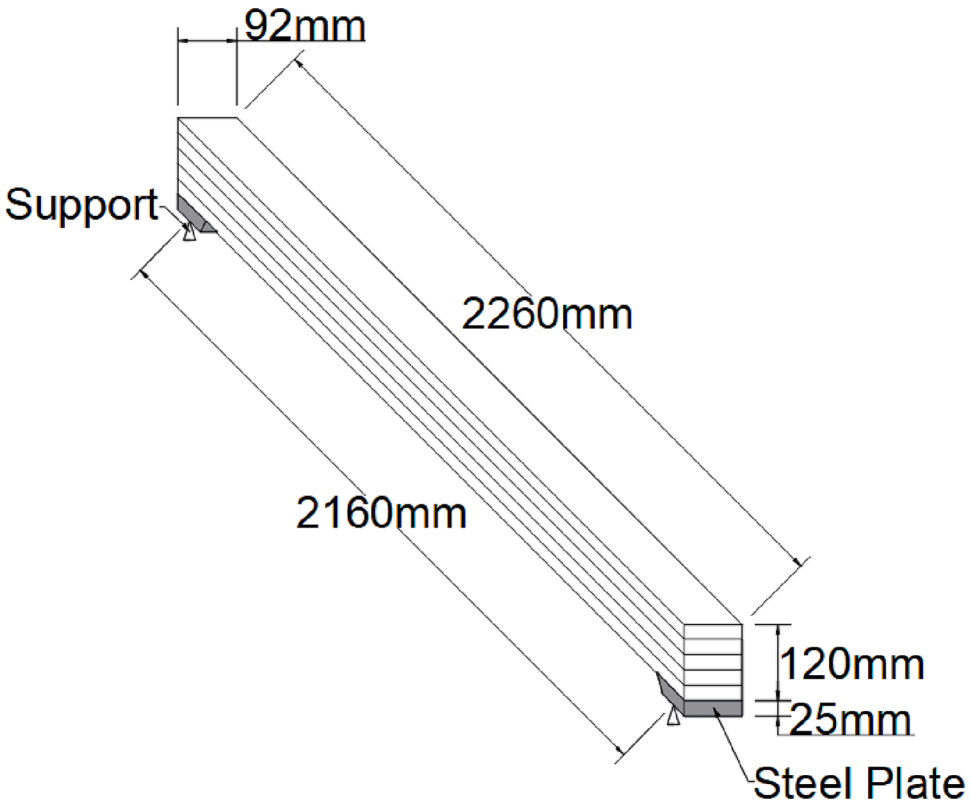

Fig. 7. Layout and dimensions of FE model for Martins's Specimens [21].

because they are proven (as will be shown later in the paper) to be much smaller than those due to flexure.

2.5. Longitudinal shear bond stress

Fig. 6 provides a free body diagram of a short portion of the joist with an excluded area as cross section, in order to mathematically define the longitudinal shear bond stress (τ) based on equilibrium. For the layered approach as shown, the excluded area's axial force F_{ea} equals the summed layer forces (based on flexural stresses) from the section base to layer number p. Scrutiny of Fig. 6 suggests that the shear bond stress τ is linearly correlated to the longitudinal gradient of F_{ea}, as proven in Equation (6).

$$F_{ea} + dF_{ea} = F_{ea} + \tau w dx \tag{6}$$

$$\tau = \frac{1}{w}\frac{dF_{ea}}{dx} \tag{7}$$

Using the chain rule of differentiation:

$$\tau = \frac{1}{w}\frac{dF_{ea}}{dM}\frac{dM}{dx} \tag{8}$$

It should be noted that dF_{ea}/dM indicates the tangent gradient of the excluded area's axial force-moment constitutive characteristic (which is conveniently obtained by differentiating the regression polynomial equation derived for that characteristic), while dM/dx is equivalent to the shear force V which develops within the member at the section of interest. Therefore:

$$\tau = \frac{1}{w}\frac{dF_{ea}}{dM}V \tag{9}$$

This equation clearly illustrates the core roles of the section constitutive characteristic (via dF_{ea}/dM), of section geometry (w) and of global equilibrium (V) in determining the shear bond stress.

3. Finite element modelling

Alongside the spreadsheet analysis, finite-element (FE) analysis was conducted to simulate the mechanical behaviours of the verification specimens using Abaqus 2021. The FE model was detailed using the same distribution of layers through the depth of the cross section as was used for the layered approach coded into the spreadsheet. The FE model also includes joist overhangs 50 mm beyond the supports and a support-load spreading steel plate which was placed underneath each end of the joist as illustrated in Fig. 7.

The FE analysis was conducted assuming quasi-static loading. The convergence criterion was based on setting a threshold for the out-of-balance nodal forces, namely the differences between the applied nodal forces and those consistent with the updated nodal displacements. 3D solid elements (C3D8) with translational degrees of freedom were used in the FE models. This refers to corporeal 3D continuum hexahedral eight-node linear-sided elements with full integration, which means that each element's overall stiffness matrix is computed at all Gauss points. This approach avoids an excessive deformation termed the 'hourglass effect'. The mesh, as shown in Fig. 8, is refined to a degree that enables both accuracy and computational efficiency. The element size within the span was $24\text{mm long} \times 11.5\text{mm thick} \times 12\text{mm wide}$, giving 8×10 elements across the width and height respectively of the cross-section.

The load condition is similar to that applied in the actual bending test, namely two line-loads applied on the upper surface of the joist at 720 mm (one third of the span) from each support. Translations were blocked in three directions at one support and in two directions (the longitudinal translation was allowed) at the other support. Relative longitudinal movement through the depth of the loaded joist is due to shear deformations of the timber. Accordingly, material shear moduli are discussed in the remaining paragraphs of this section. However, there is zero slip at the adhesively bonded glulam interfaces [20], and so tie constraints were adopted in the FE model to disallow relative motion at the contact surfaces between lamellas and at each support's timber joist - steel plate interface.

Like the spreadsheet analysis, along-grain uni-axial stress–strain relationships were used to characterise the material in the FE model. Timber is an anisotropic material, and its mechanical properties are usually defined in three directions: longitudinal (L), radial (R) and tangential (T). The material is mainly subject to compression or tension in the longitudinal direction in this study, therefore the primary aim is to

Table 4
Input data for FE analysis.

	E_r(MPa)	E_t(MPa)	G_{lr}(MPa)	G_{lt}(MPa)	G_{rt}(MPa)
BP	890.7	458.1	768.6	615.9	112.0
MP	1735.6	922.9	1281.0	1115.7	261.7
BG	2123.3	823.3	2036.7	1451.7	542.7

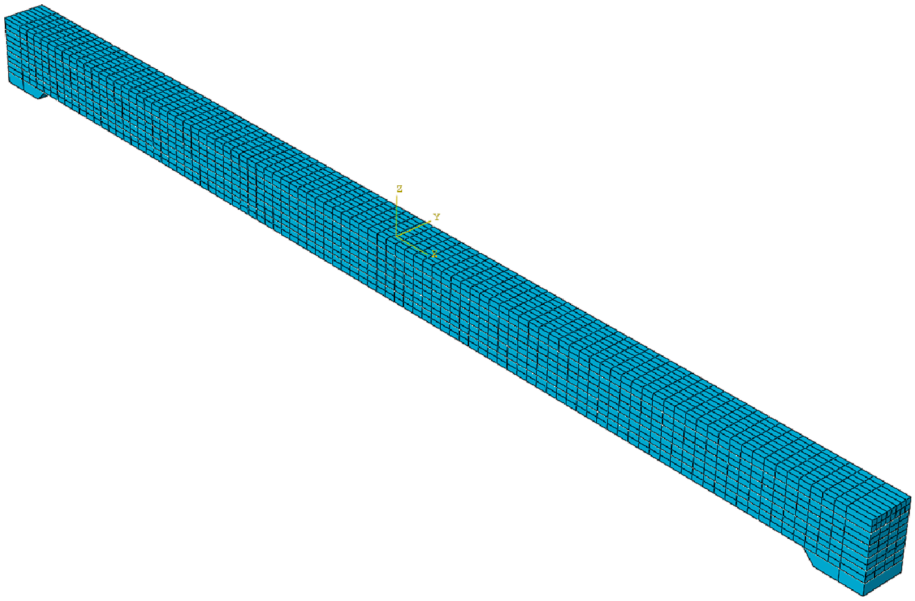

Fig. 8. Abaqus Finite element model of Martins's glulam joist [21].

describe the mechanical behaviour in the longitudinal direction in both elastic and plastic regimes. Since the timber species considered in this study only exhibit nonlinearity under compression in the longitudinal direction, it was necessary to develop a subroutine to describe the mechanical behaviours of the ductile timber species. The stress–strain relationships used in the longitudinal direction were consistent with those defined earlier for the spreadsheet analysis. The values of other elastic constants were adopted from Martins [21], which in turn was summarised from the available data in the previous literature and in existing standards [25–27].

These led to the shear moduli shown in Table 4, which are essential to run the FE analysis to describe the shear behaviours of the materials along the three key axis directions. However, the spreadsheet approach doesn't need the shear moduli because the materials are assumed to be shear-rigid. Later, comparisons will be presented between the spreadsheet and FE results, thereby making it possible to identify that the impact of excluding the shear moduli is not significant. Similar considerations for the study by Tomasi et al [23] will be discussed later.

4. Verification study - specimens tested by Martins

Martins [21] fabricated and tested hybrid glulam joists comprising three different combinations of the timber species maritime pine (MP), poplar (BP) and blue gum (BG). Table 4 gives the relevant material properties not previously given in this paper for all three species. As Fig. 9 shows, the stacking sequences of the 24 mm thick, 92 mm wide lamellas varied between the three joist sections, but in all cases five lamellas were used to give an overall section depth of 120 mm. Each section used two species, with a symmetric distribution of material about the middle lamella for sections H1 and H3, but asymmetric for H2. Fig. 10(a) shows that each joist, of 2.16 m span, was loaded at the third points of the span in 4-point bending.

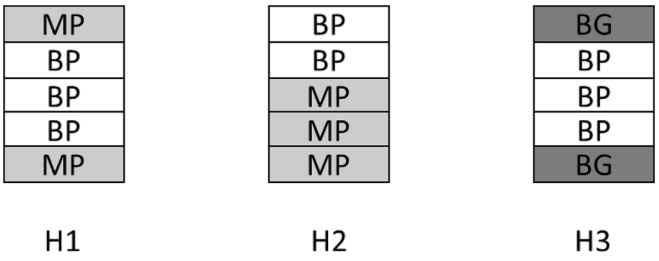

Fig. 9. Layout of hybrid sections.

Exploiting symmetry about midspan in Fig. 10(a), the spreadsheet-implemented computations have been applied to the half-span cantilever rooted at midspan and with loading as shown in Fig. 10(b). Calculation sections were spaced at 5 mm centres (2.3% of the span) in the longitudinal direction. In what follows, the resulting full range load vs deflection predictions from the spreadsheet and from the FE analyses are verified by comparison with the corresponding test data from Martins [21]. The spreadsheet is then further verified by comparing its predicted longitudinal shear stresses well into the nonlinear regime with the corresponding FE results.

Subsequently, in the following Sections of the paper, further results from the verified spreadsheet will be used to explain other facets of nonlinear response (flexural stiffnesses and stresses, longitudinal shear stress profiles, etc) not only for the present 4-point loads, but also for uniformly distributed loading on the joist. Parallel FE results will be used to deepen confidence in the spreadsheet approach and to reinforce insight into the nonlinear behaviours of these ductile hybrid engineered timber joists.

4.1. Member deflection

Fig. 11 compares experimental and predicted total load [2P on Fig. 10(a)] vs midspan deflection behaviours. The test data show that all hybrid members exhibited pronounced elasto-plastic nonlinearities at advanced stages of loading, also that the three members tested within

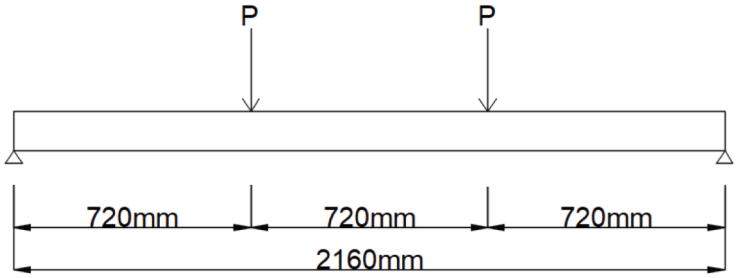

(a)

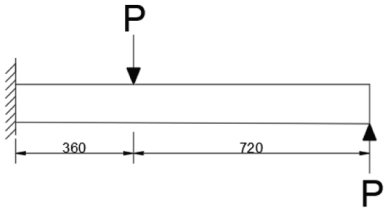

(b)

Fig. 10. Point load case: (a) joist test setup (b) cantilever for computational model.

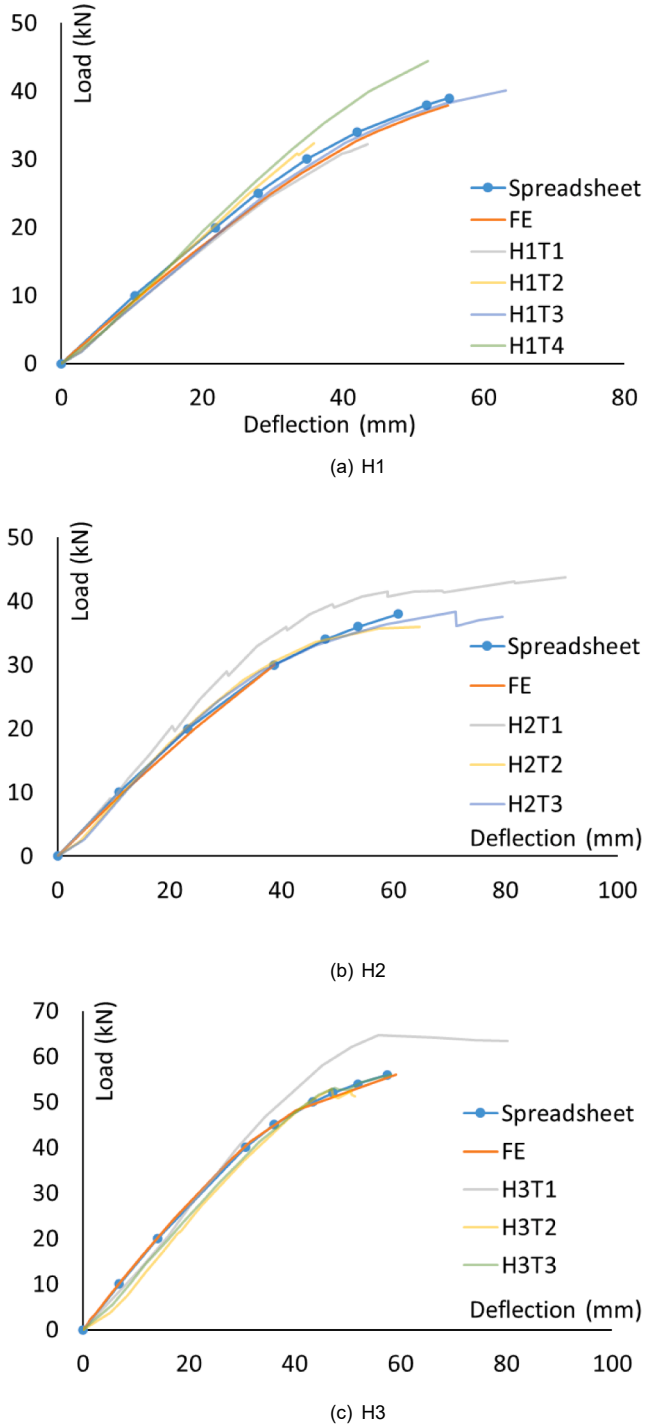

Fig. 11. Verification via Load-Deflection Plots for Martins [21].

Table 5
Spreadsheet predictions compared with test results & FE predictions.

Spreadsheet	Average Ordinate Ratio		Ultimate Load Ratio	
	Experiment	FE	Experiment	FE
H1	0.947	0.915	0.956	1.026
H2	0.999	0.973	1.029	1.018
H3	0.950	1.048	1.015	1.029

each group showed reasonably consistent behaviour with each other.

The spreadsheet and FE predictions correlate nicely with the test data well into the nonlinear regimes for all three hybrid members. Notably, the predictions capture the eventual levelling off of the experimental load–deflection curves particularly for section H2, signifying a good predictive capability to replicate truly ductile behaviour. The reliable predictions are further evidenced in Table 5, which shows two ratios used to check the fidelity of the predictions. One ratio focuses on the full range load–deflection behaviour from the unloaded state to failure, and refers to the average ordinate ratios, namely the ratios between ordinates for given abscissae on the spreadsheet and test or FE plots. It is seen that the values are close to 1.0. The second ratio focuses on comparing the predicted and test failure loads, which is also seen to closely approximate 1. In addition, according to the spreadsheet and FE predictions, all the hybrid joists failed by fracture at the base in the midspan zone, which is consistent with experimental results.

Fig. 12(a) shows that, at the ultimate loads, the spreadsheet results reveal pronounced monotonic reductions of section flexural stiffness between the supports and the applied load locations. This reduction was particularly striking over short lengths immediately adjacent to the point loads, with a highly significant 27.9% drop in stiffness occurring over only 8.3% of the span for H3. Fig. 12(b) zooms in on this region and shows that the section spacing of 5 mm used for the spreadsheet computations is eminently suited to capturing this variation. This in turn enables reliable computation of deflections and internal stresses.

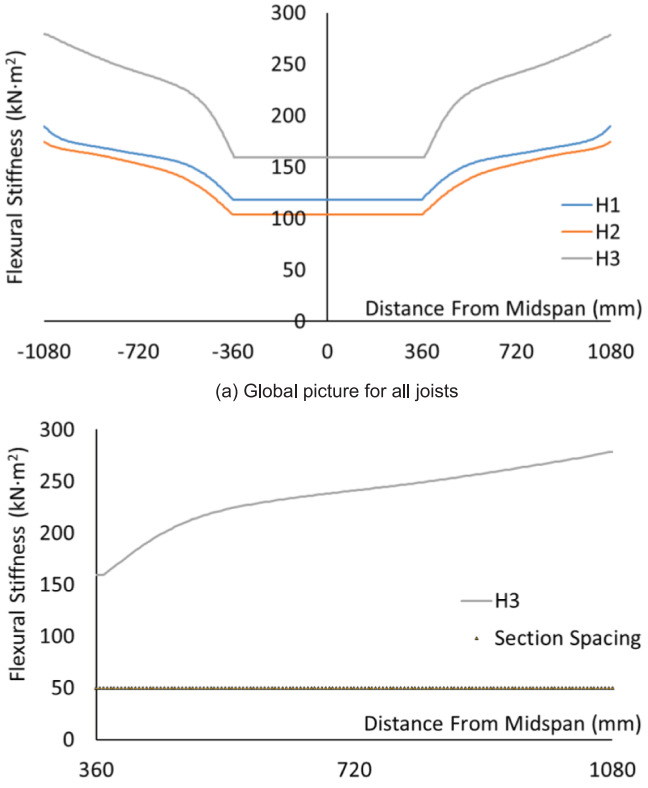

Fig. 12. Stiffness profiles along joists at ultimate.

Table 6
Comparing shear and flexural deflections.

Section	δ_{max} (mm)	Unfavourable $\delta_{s,max}$ (mm)	$\delta_{s,max}/\delta_{max}$(%)
H1	55.05	2.65	4.81
H2	60.81	2.65	4.35
H3	57.54	1.61	2.81

4.2. Shear deflection

It is now shown that, at the ultimate loading, the shear deflections ($\delta_{s,max}$) of the joists H1-H3 are negligible relative to the flexural deflections (δ_{max}) predicted by the spreadsheet computations. To that end it is difficult to determine the shear modulus G of composite sections, so instead the shear deflections are determined for sections of uniform material (the lower shear modulus of the two materials on the actual section) and of the same dimensions as the analysed joists. The shear deflection is calculated based on Equation (10) from Ross [24].

$$\delta_s = \frac{6}{5}\int_0^L \frac{V}{AG}dx \tag{10}$$

Table 6 compares the resulting shear and flexural deflections at ultimate loading. The maximum $\delta_{s,max}/\delta_{max}$ ratio is found for H1 at only 4.8%. This confirms that little error has been introduced by neglecting shear deflections.

4.3. Longitudinal shear bond stress

Fig. 13 verify the spreadsheet predictions of longitudinal shear stress by showing that they compare well with the corresponding FE results at the section height of maximum shear stress (which will be explained later in Section 6.0 and Fig. 17 of this paper) for the ultimate load. Fig. 13 refer to the left-hand halves of the spans, noting that the longitudinal shear stress along the entire member is anti-symmetric about midspan. The spreadsheet-predicted peak shear stresses vary from 3.95 N/mm^2 for H1 to 6.20 N/mm^2 for H3, reflecting the very different make-ups of the joists.

Table 7
Longitudinal shear stress comparisons between spreadsheet and FE.

Section	Peak Shear Stress Ratio	Average Ordinate Ratio	Standard Deviation of Average Ordinate Ratio
H1	1.292	1.101	0.220
H2	1.353	1.152	0.242
H3	1.260	1.035	0.225

As Table 7 shows, the spreadsheet results compare well with the FE ones, with average ordinate ratios (namely ratios of shear stress ordinates for given horizontal distance abscissas) in the range 1.035–1.152, and with peak shear stress ratios (relative to the FE-predicted ones) in the range 1.26 – 1.35 which puts the spreadsheet predictions on the safe side. The results show almost constant longitudinal shear stress in the linear zones near the supports, but this changes to highly nonlinear variations in the elasto-plastic zones near the applied loads. Note that very near the point load locations the spreadsheet predicts a small spike (due to the assumption of infinite shear modulus) in longitudinal shear stress, while the FE approach (which assumes finite shear moduli) gives slightly more rounded peaks quite near the point loads. For all three sections, the longitudinal offset between the FE and spreadsheet predicted shear stress peaks along the member is 72 mm, only 3.3% of the beam span. This provides ready further evidence of the high quality of

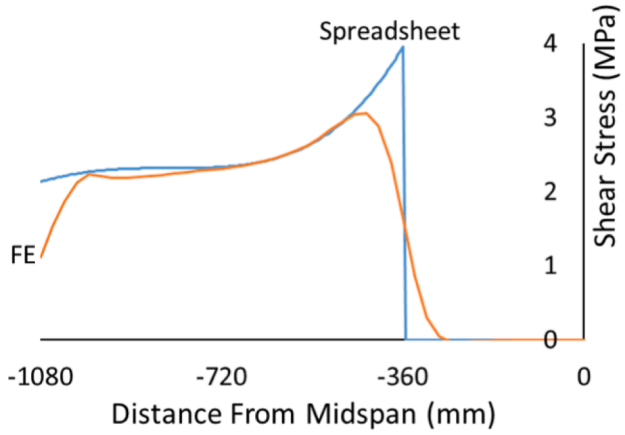

(a) H1 at P=19.5kN, h=35mm

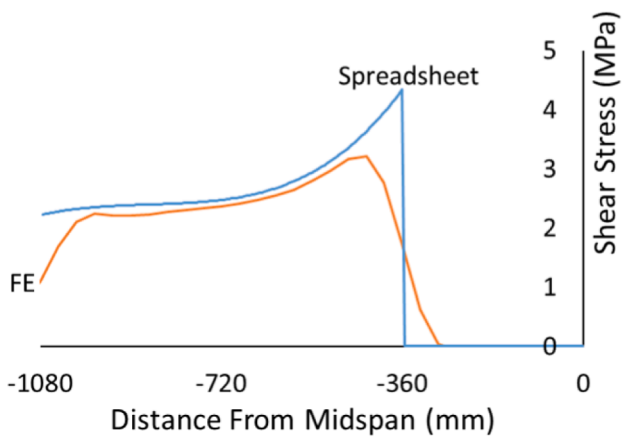

(b) H2 at P=19kN, h=37mm

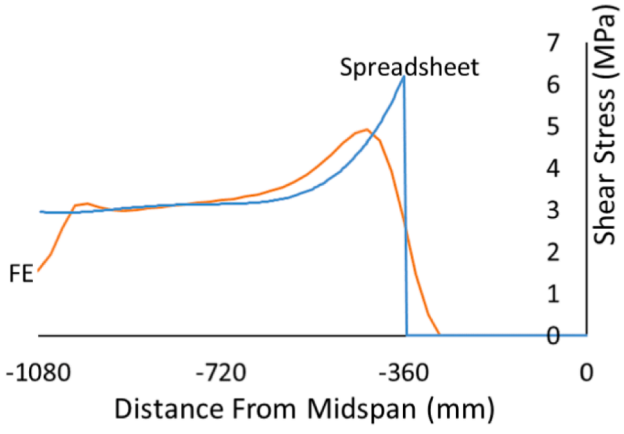

(c) H3 at P=28kN, h=29mm

Fig. 13. Predicted longitudinal shear stress profiles at ultimate load for Martins [21].

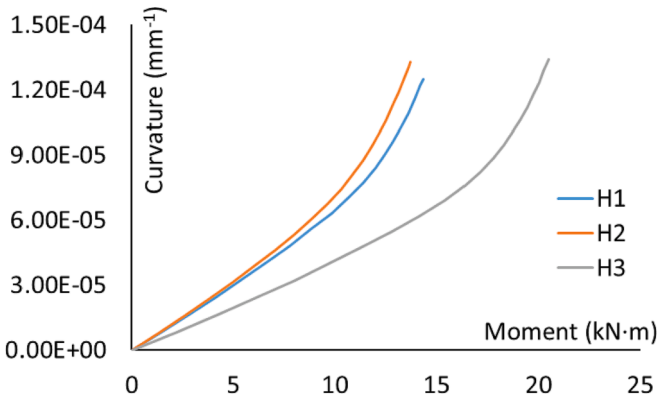

Fig. 14. ($\kappa - M$) Characteristics for Martins's specimens [21].

Table 8
Regression equations for ($M - \kappa$) Characteristics.

H1	$\kappa = 3.919861 \times 10^{-10}M^5 - 8.441922 \times 10^{-9}M^4 + 6.099480 \times 10^{-8}M^3 - 8.216532 \times 10^{-8}M^2 + 5.692 \times 10^{-6}M - 1.625092 \times 10^{-9}$
H2	$\kappa = 4.294296 \times 10^{-10}M^5 - 8.655368 \times 10^{-9}M^4 + 6.547106 \times 10^{-8}M^3 - 9.497277 \times 10^{-8}M^2 + 5.985933 \times 10^{-6}M + 1.137737 \times 10^{-8}$
H3	$\kappa = 1.916947307 \times 10^{-10}M^5 - 7.516373 \times 10^{-9}M^4 + 1.039180 \times 10^{-7}M^3 - 5.334634 \times 10^{-7}M^2 + 4.721274 \times 10^{-6}M - 1.335811 \times 10^{-7}$

the spreadsheet predictions.

5. Nonlinear stiffness considerations

Fig. 14 shows the $\kappa(M)$ constitutive behaviours of the three sections, with the associated regression equations summarised in Table 8. Note that the curvatures of the order of 10^{-5} mm^{-1} seen in Fig. 14 are comparable to those shown for timber members in another study by Tomasi et al. [23], also used for verification later in the present paper.

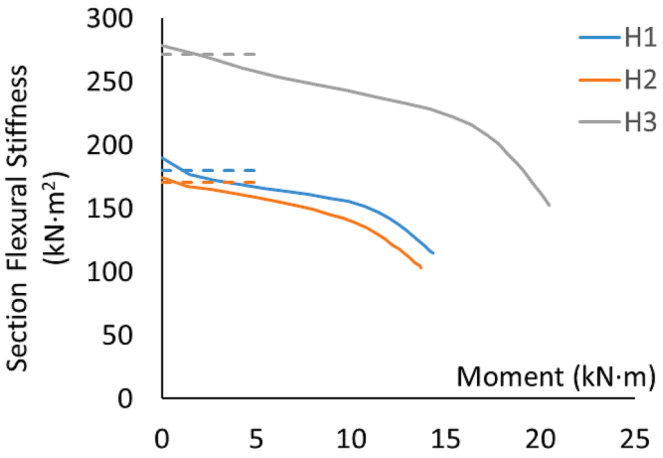

Fig. 16. Section flexural stiffness as a function of moment.

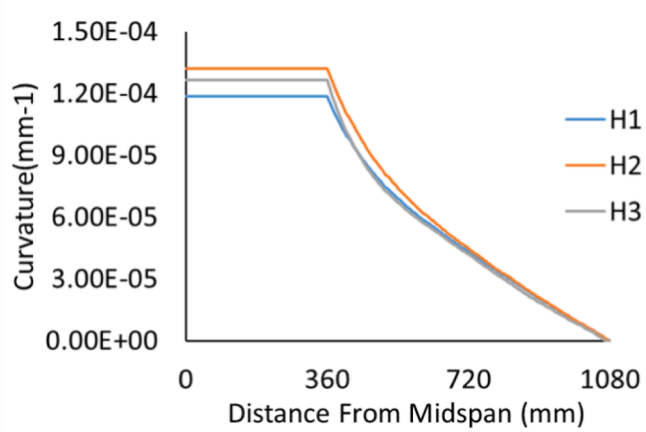

(a) Curvature Profile

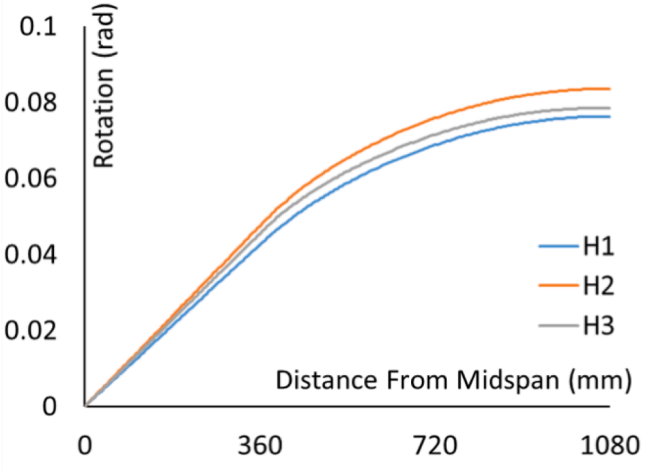

(b) Rotation Profile

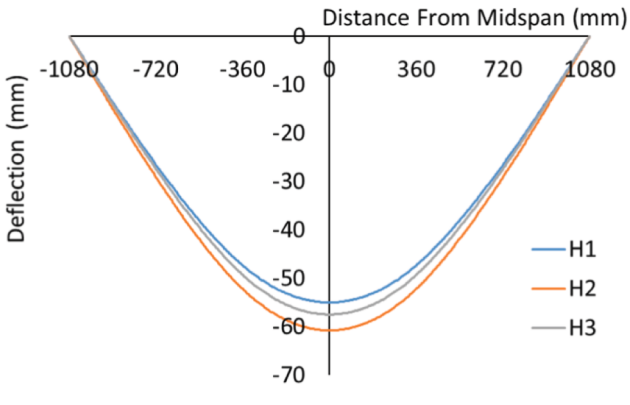

(c) Deflection Profile

Fig. 15. Spreadsheet Predictions of Curvature to Deflection Profiles at Ultimate Loading.

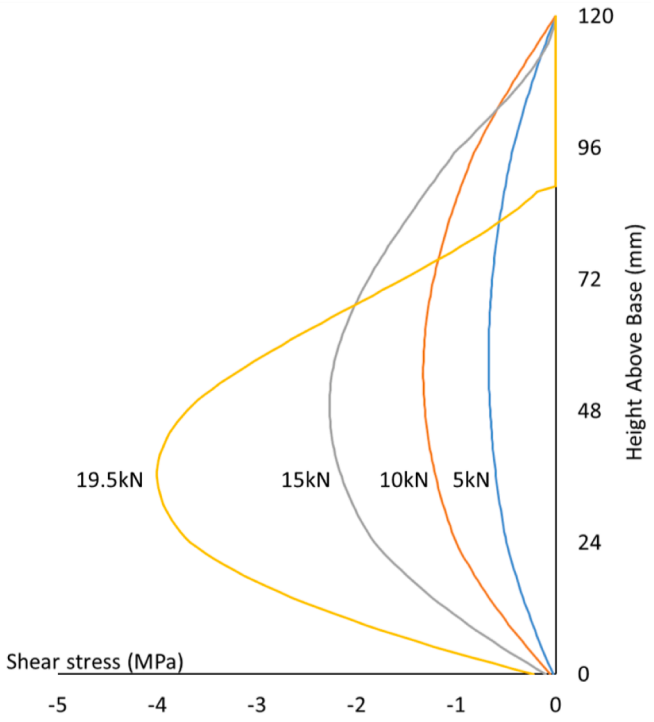

(a) H1

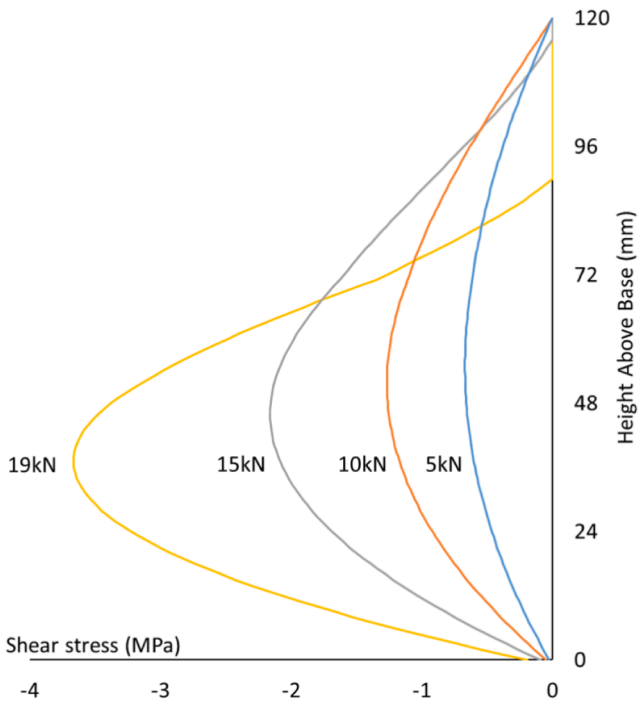

(b) H2

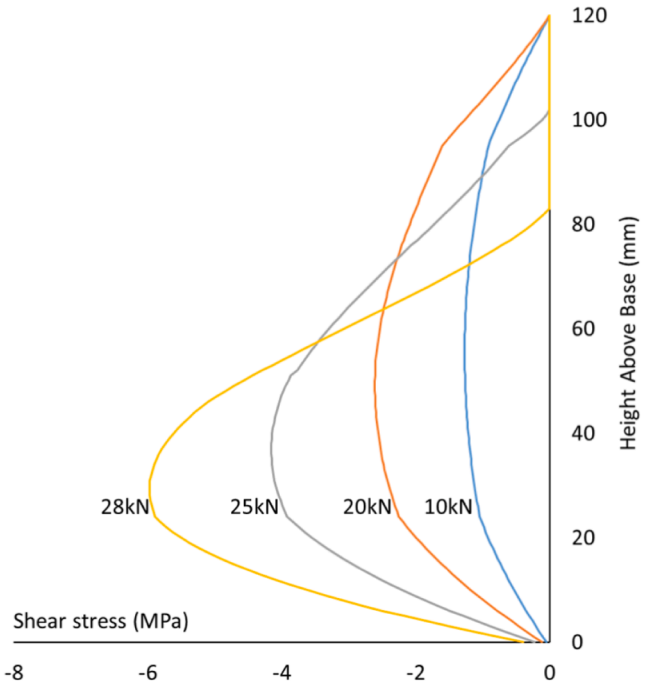

(c) H3

Fig. 17. Through-depth shear stress distributions at loaded sections.

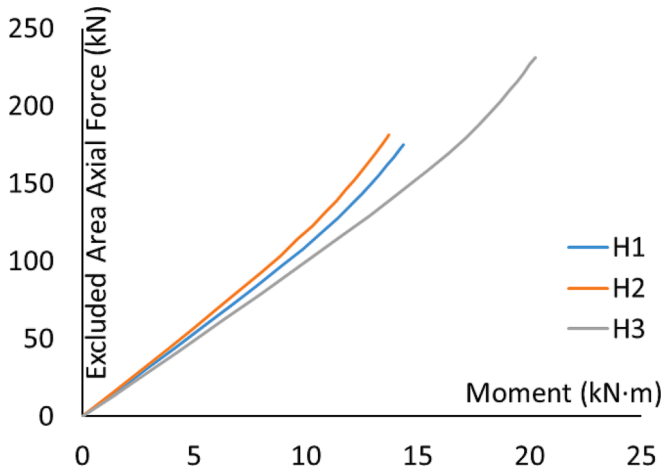

Fig. 18. Excluded area axial force versus moment for Martins [21].

Table 9
Regression equations $F_{ea} = f(M)$ and the differential equations dF_{ea}/dM:

H1	$F_{35} = 6.101240 \times 10^{-5}M^5 + 4.712930 \times 10^{-4}M^4 - 0.02509462M^3 + 0.2328537M^2 + 10.058135697M + 0.03458221\frac{dF_{35}}{dM} = 3.05062 \times 10^{-4}M^4 + 1.8965172 \times 10^{-3}M^3 - 0.07528386M^2 + 0.4657146M + 10.058135697$
H2	$F_{37} = 3.299013 \times 10^{-5}M^5 + 1.43136 \times 10^{-3}M^4 - 0.02920462M^3 + 0.2278896M^2 + 10.76619M + 0.05133393\frac{dF_{37}}{dM} = 1.6495065 \times 10^{-4}M^4 + 5.72544 \times 10^{-3}M^3 - 0.08761386M^2 + 0.4557792M + 10.76619$
H3	$F_{29} = 6.712334 \times 10^{-5}M^5 - 2.15642 \times 10^{-3}M^4 + 0.02245049M^3 - 0.03923684M^2 + 9.63295M - 0.05003387\frac{dF_{29}}{dM} = 3.356167 \times 10^{-4}M^4 - 8.625680 \times 10^{-3}M^3 + 0.067351455M^2 - 0.078473686M + 9.632950048$

Combination of Fig. 14 with the moment diagrams for joists H1-H3 at the ultimate loads led to the curvature diagrams of Fig. 15(a) which, on double integration produced the rotation and deflection profiles of Fig. 15(b), (c). The highly curved deflection profiles in the midspan zones are reminiscent of plastic hinges.

For any level of moment on any of the hybrid timber sections, the equivalent section flexural stiffness EI is derived as $EI = M/\kappa$. Based on the present computational (spreadsheet) approach, the $EI(M)$ curves are presented in Fig. 16. Added to this Figure are short-dashed lines extending across low values of moment to indicate the theoretical section EI values calculated using transformed section theory based on linear behaviour and proceeding by way of the parallel axis theorem.

Comparing the dashed lines and the solid curves, it is evident that the nonlinear compression softening has a dominant influence on section stiffness even at modest values of bending moment. The particularly sharp drops in stiffness which occur near the ultimate moments account for the similar sharp drops in stiffness along the span near the locations of peak moment in Fig. 12.

6. Longitudinal shear bond stress

Fig. 17 illustrates the through-depth distribution of longitudinal shear bond stress at the joist sections immediately below the load points, for different load levels between 25.6% and 100% of ultimate. The plots clearly show through-depth redistribution of stresses (driven by the material compression nonlinearity) especially at higher loads. Observe that at the highest load for H1 and at the two highest loads for H2, H3, the longitudinal shear stress is identically zero in the upper zones of the sections. This is precipitated by the compressive stress having reached the ductility plateau along the joists in those zones. Under such circumstances, and as can be seen in the Figures, the maximum shear stresses were found to occur in the lower reaches of the sections, namely at h = 35 mm for H1; h = 37 mm for H2 and h = 29 mm for H3. It is the longitudinal shear stresses along horizontal planes at these heights above the bases that are plotted in Fig. 13.

For each joist, Fig. 18 shows the $F_{ea}(M)$ constitutive characteristic for the excluded area bounded by the horizontal plane of maximum shear stress, while Table 9 provides the associated regression equations.

Fig. 19 presents the longitudinal shear profiles calculated by spreadsheet at different load levels based on Equation (9). The corresponding FE results are plotted in Fig. 20. Within the nonlinear zone, the present computational framework shows a growing spike in the longitudinal shear stress profile at the load point, which compares with similar FE results of a slightly rounded peak in the same zone.

Fig. 21 compares the maximum shear stresses along the member from the spreadsheet and FE analyses, plotted against applied load P. There is a good similarity between the two curves, with only moderate disparity between the results during the more advanced stages of nonlinearity, where local shear deformations influence the FE-predicted maximum shear stress near the load point while the spreadsheet approach assumes a shear-rigid member, which is illustrated in Section 4, Fig. 13.

7. Nonlinear flexural stress distribution

Fig. 22 compares the spreadsheet- and FE-predicted through-depth bending stress distributions at 40%, 80%, and 100% of section moment capacity. The steps occur at changes of timber species. Otherwise, notice how the distribution remains linear within the tensile zone, but progresses from linear to increasingly nonlinear above the neutral axis due to compression softening of the material there with increasing moment especially near failure. The FE results are also plotted, showing very good agreement.

For all three section layouts H1-H3, section failure occurs via fracture of the extreme tensile (base) fibre, by which stage the bending stress is constant in the top zones of the section owing to “yield” of the compression material.

8. Uniformly distributed load cases

For completeness, the spreadsheet results are compared with the FE ones also assuming a Uniformly Distributed Load (UDL), which is a common design load type. The results show that nonlinearity is not profoundly observed for the UDL cases, and so only the UDL case of H3 is here used to exhibit the correctness of the spreadsheet analysis alongside the powerful FE tool. Figs. 23, 24 compare, respectively, the load–deflection curves and the longitudinal shear bond stress plots at both low load and ultimate load to illustrate the effect of material nonlinearity on member behaviour.

The excellent spreadsheet-FE correlation further verifies the power of the present computational approach. In Fig. 24, note that the variation of shear bond stress along the member changes from almost linear at low load to a gentle bump near midspan indicating nonlinearity in that zone at ultimate load.

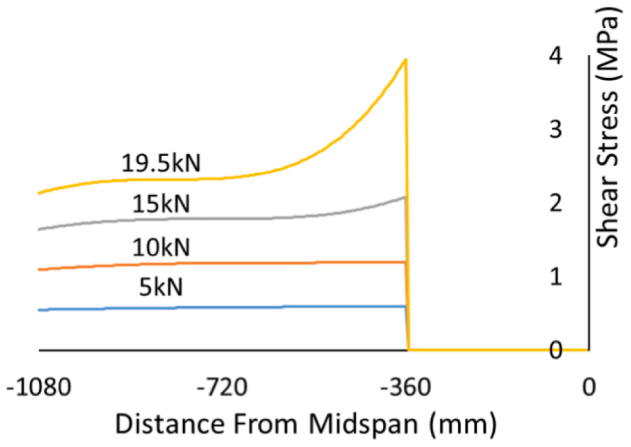

(a) H1 at 35mm

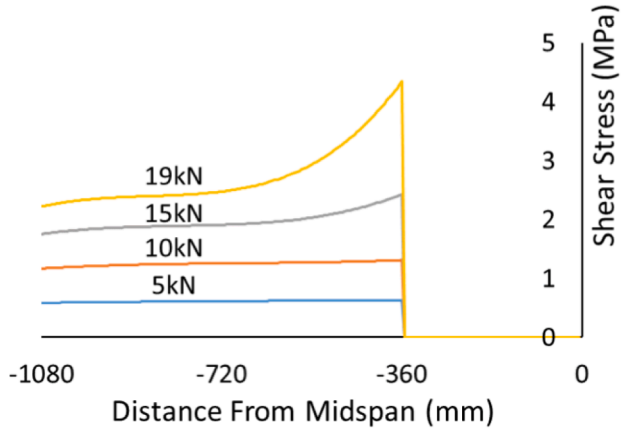

(b) H2 at h=37mm

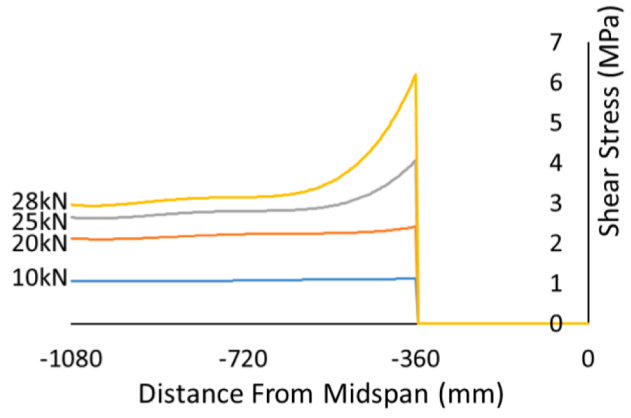

(c) H3 at h=29mm

Fig. 19. Longitudinal shear stress from spreadsheet analysis for Martins [21].

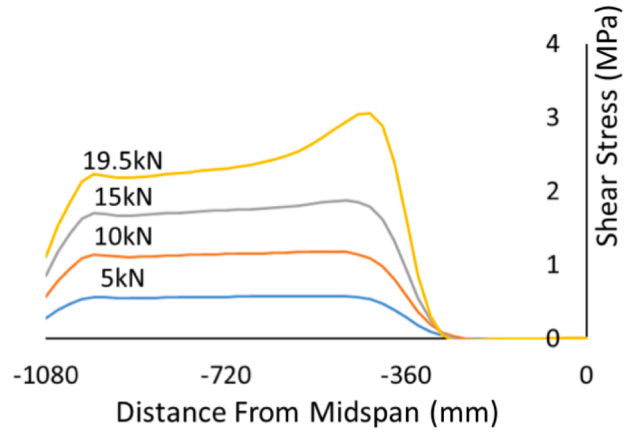

(a) H1 at h=35mm

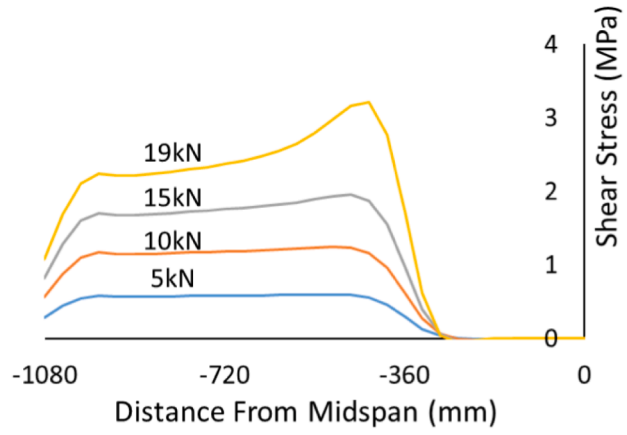

(b) H2 at h=37mm

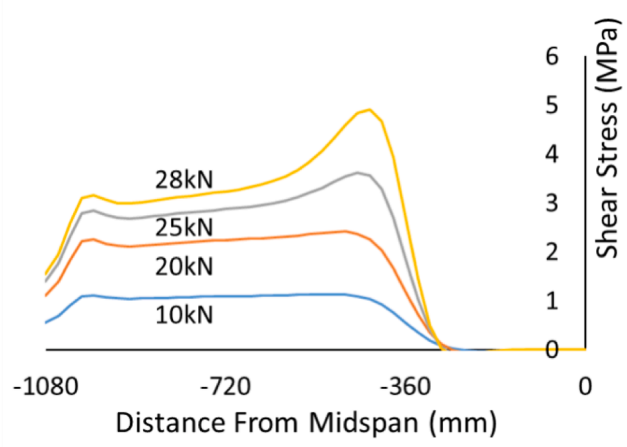

(c) H3 at h=29mm

Fig. 20. Longitudinal shear stress from FE analysis for Martins [21].

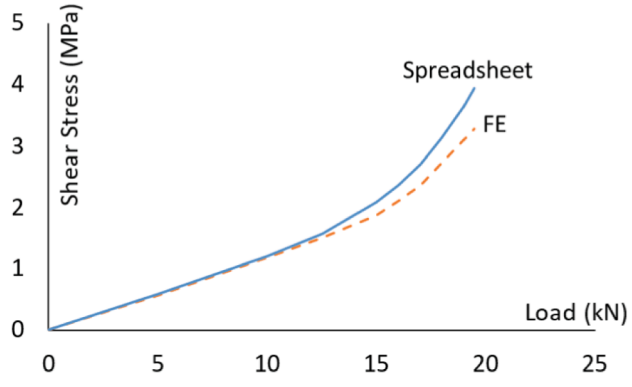

(a) H1 at h=35mm

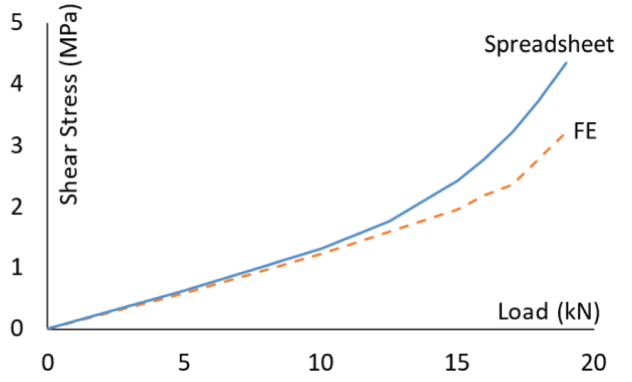

(b) H2 at h=37mm

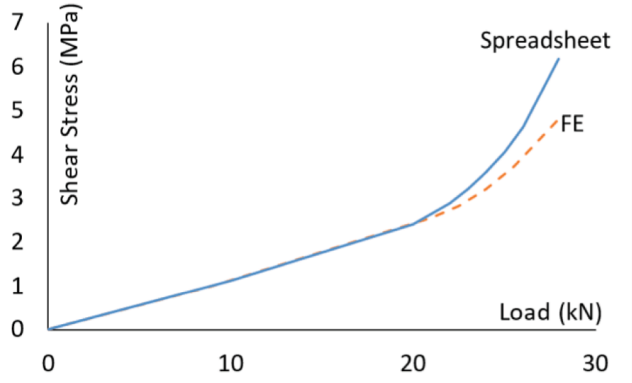

(c) H3 at h=29mm

Fig. 21. FE and Spreadsheet maximum shear stress variations with load.

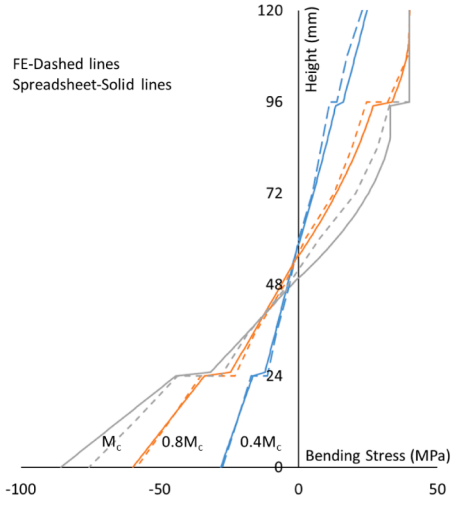

(a) H1

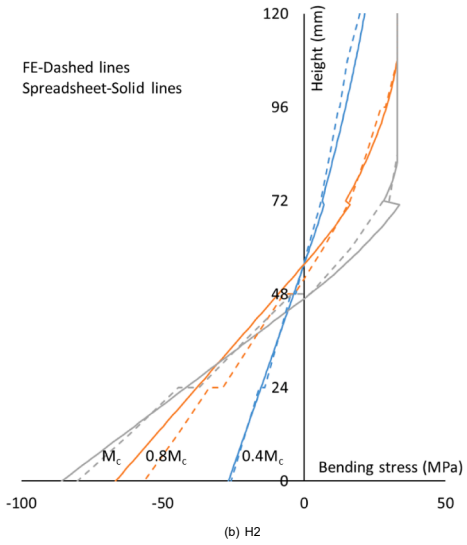

(b) H2

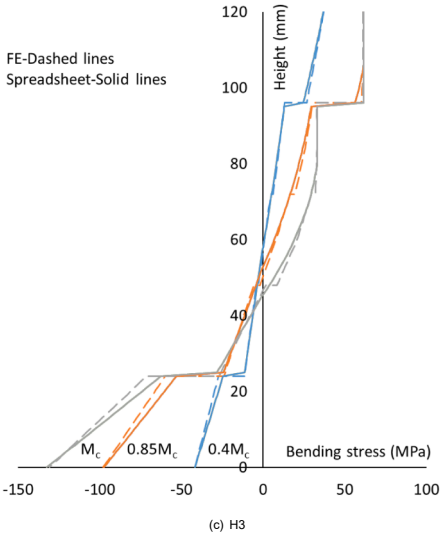

(c) H3

Fig. 22. Through-depth bending stress distributions.

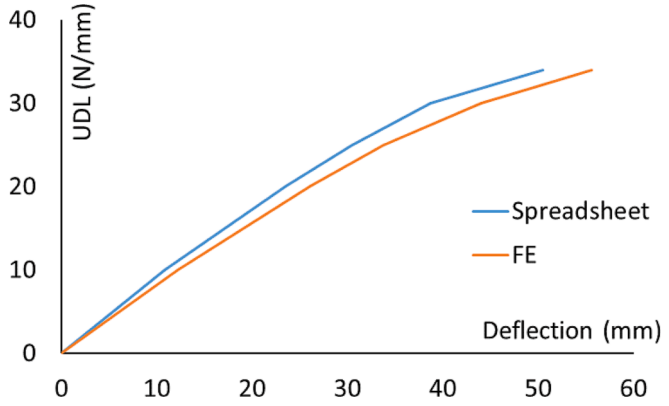

Fig. 23. Joist H3 UDL against maximum deflection along the joist.

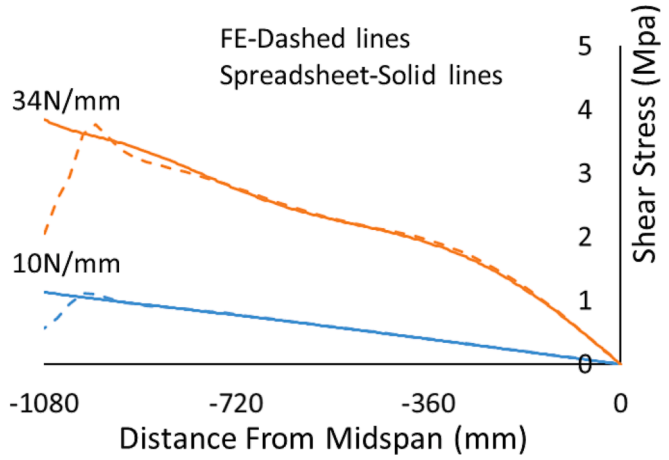

Fig. 24. Longitudinal shear stress for H3 at h = 29 mm under UDL.

9. Case study of Tomasi et al.

9.1. Experimental setup

In this section the computational framework is further validated using a study by Tomasi et al. [23], which output experimentally derived *M-κ* plots from four-point bending tests on poplar-larch hybrid beams. The midspan section moment was obtained via equilibrium for the loaded beam, while curvature was determined as the through-depth gradient of the recorded longitudinal strains.

The hybrid beam's laminations were each 80 mm wide, 10.5 mm thick, 2000 mm long. Fig. 25(a) shows there were nine poplar lamellas above two larch lamellas. Fig. 25(b) shows the loads applied at the third points of the span. Fig. 25(c) shows the loaded cantilever model used for the computations.

9.2. Material and section constitutive behaviours

The material constitutive behaviours of poplar and larch under compression are here defined by the Glos model [16,17], namely the generic Equation (11).

$$\sigma = \frac{\varepsilon + k_1\varepsilon^4}{k_2 + k_3\varepsilon + k_4\varepsilon^4} \tag{11}$$

in which

$$k_1 = \frac{f_{c,0,u}}{3E_{c,0}\varepsilon_{c,0}^4(1-\frac{f_{c,0,u}}{f_{c,0}})} \tag{12}$$

$$k_2 = \frac{1}{E_{c,0}} \tag{13}$$

$$k_3 = \frac{1}{f_{c,0}} - \frac{4}{3E_{c,0}\varepsilon_{c,0}} \tag{14}$$

and finally

$$k_4 = \frac{1}{3E_{c,0}\varepsilon_{c,0}^4(1-\frac{f_{c,0,u}}{f_{c,0}})} \tag{15}$$

For clear poplar, Fig. 26 shows Tomasi's experimentally obtained compressive stress–strain plot, with a peak stress of 25 MPa, along with the closely-fitting Glos curve used in this study. Within the context of a parametric study, a Glos curve based on a peak compressive stress of 30 MPa was also used. Fig. 27 shows the tension and compression properties of the larch and (both 25 / 30 MPa compressive strength versions of the) poplar, as input to the spreadsheet and FE analyses.

Table 10 gives the materials' parallel-to-grain mechanical constants. Table 12 gives those for the transverse and vertical directions (input to the FE) for larch, sourced from Liu et al. [28]. The elastic constants for poplar were those from Martins [21].

9.3. Finite element modelling for Tomasi et al.

The FE model contained the same layout of 11 lamellas through the depth of the hybrid timber joist as the actual member. The element size was set at 30mm length × 10.5mm thickness × 20mm width, to give the mesh distribution shown in Fig. 28(a). Concentrated loads are applied at the 1/3rd span locations from the supports. The analysis setups and boundary conditions were the same as used in the FE modelling for Martins [21]. The deformed shape of the model at ultimate is shown in Fig. 28(b).

9.4. Validation of load–deflection and longitudinal shear bond stress

Fig. 29 compares the spreadsheet- and FE-predicted *M-κ* curves with the corresponding test plot from Tomasi et al [23]. Regarding the 25 MPa spreadsheet plot relative to the test data, Table 12 shows impressive statistics of 0.847 and 0.838 for the average ordinate and ultimate moment ratios. Further evidence of the power of the spreadsheet approach. The statistics improve slightly for the FE and a bit more when the assumed poplar compressive strength increases to 30 MPa. Note also that the predicted curves mimic the pronounced elasto-plastic nonlinearities exhibited by the test curve at higher moments.

Fig. 30 shows the spreadsheet $\kappa(M)$ plot and two regression equations based on a 30 MPa compressive strength. Both equations are of the sixth order, for better approximation due to the pronounced nonlinearity of the curve.

Fig. 31 shows good agreement between the spreadsheet and FE load–deflection curves, with an average ordinate ratio of 0.954 and ultimate load ratio of 1.001.

Fig. 32 further shows good spreadsheet-FE agreement on the longitudinal shear stress profile at ultimate load, with an average ordinate ratio of 0.938 and standard deviation of 0.197. The longitudinal offset

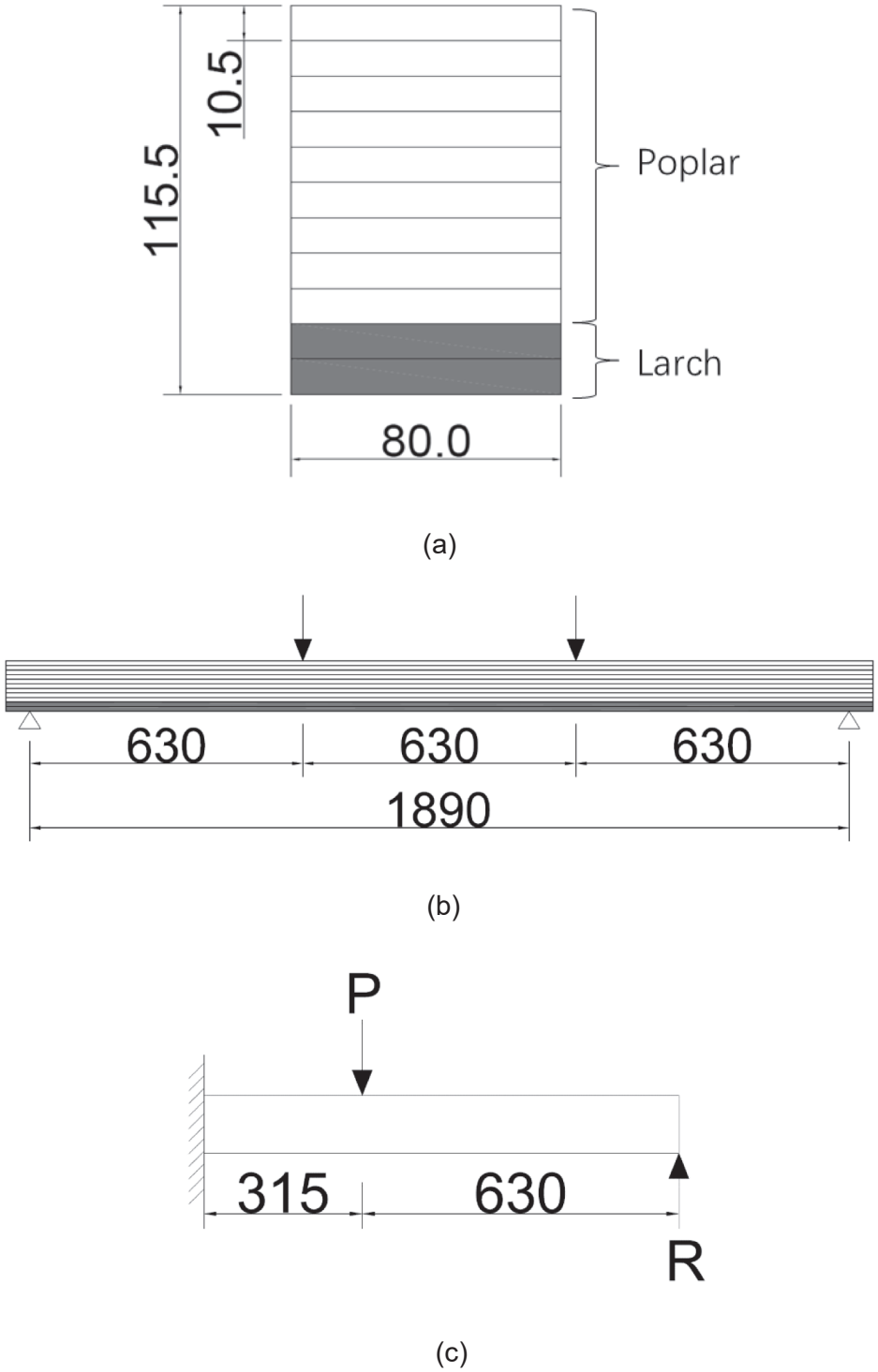

Fig. 25. Poplar-larch hybrid timber beam - (a) Stacking sequence in section (dimensions in mm) (b) Elevation (c). Cantilever computational model.

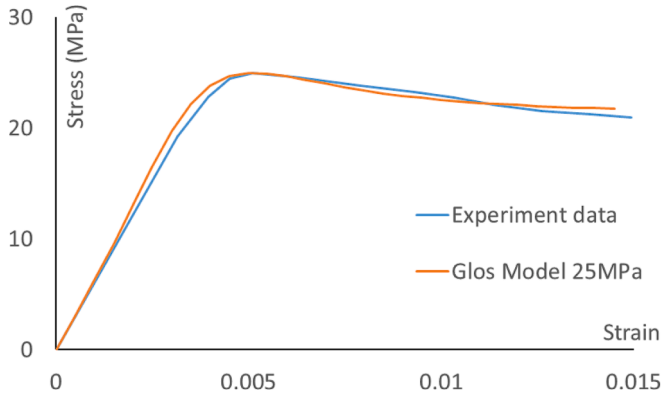

Fig. 26. Poplar material test data (Tomasi [23]) and Glos model.

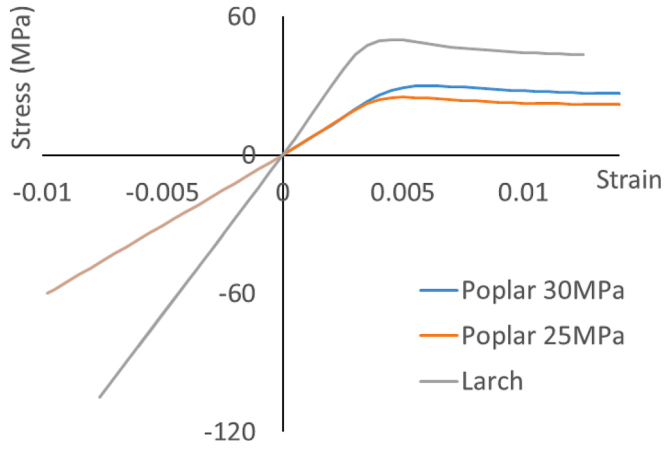

Fig. 27. Material constitutive behaviour for Tomasi et al. [23].

Table 10
Longitudinal mechanical properties for timber species (Tomasi [23]).

	Poplar (30 MPa)	Poplar (25 MPa)	Larch
Compressive Strength (MPa)	30	25	50
Elastic modulus (GPa)	6.115	6.115	13.8
Tensile Strength (MPa)	60	60	105
Crushing Strain	0.0145	0.0145	0.0125
Fracture Strain	0.0098	0.0098	0.0076

Table 11
Transverse and vertical larch material properties Tomasi et al. [23].

	E_r(MPa)	E_t(MPa)	G_{lr}(MPa)	G_{lt}(MPa)	G_{rt}(MPa)
Poplar	890.7	458.1	768.6	615.9	112.0
Larch	342.0	282.0	556.0	446.0	430.0

Table 12
Spreadsheet predictions compared with test results.

	Average Ordinate Ratio	Ultimate Moment Ratio
Spreadsheet 25Mpa	0.847	0.838
Spreadsheet 30 MPa	0.911	0.982
FE 25 MPa	0.894	0.806
FE 30 MPa	0.967	0.985

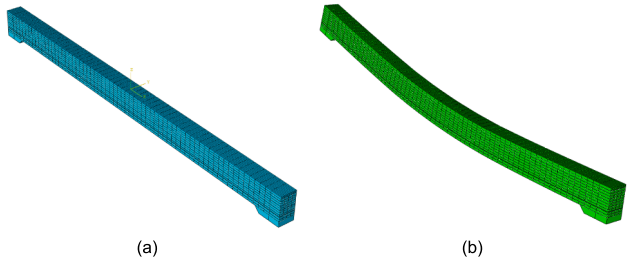

Fig. 28. Tomasi et al. [23] - (a) FE model of glulam joist (b) Deflected shape.

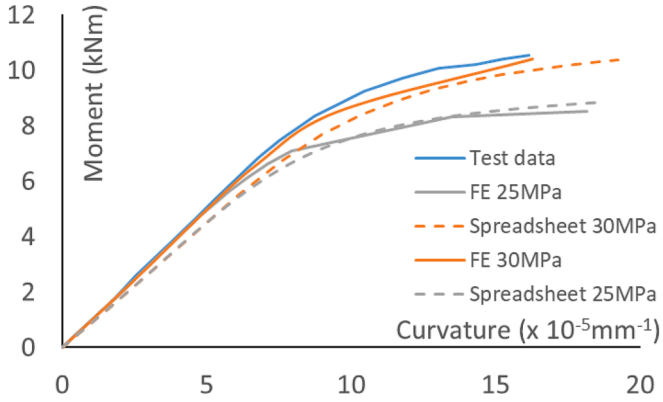

Fig. 29. Comparing spreadsheet predictions with test data, Tomasi et al. [23].

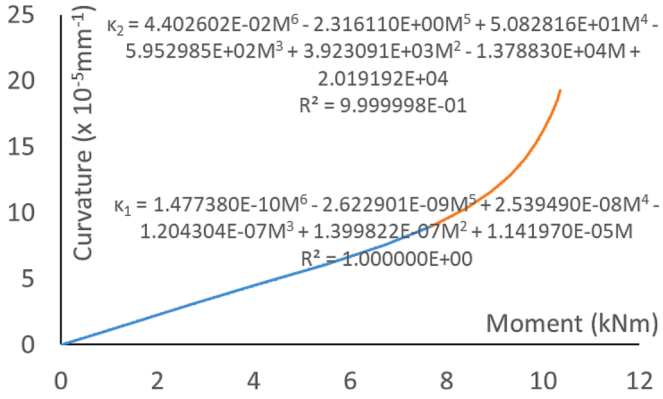

Fig. 30. $k-M$ plot and regression equations for Tomasi et al. [23].

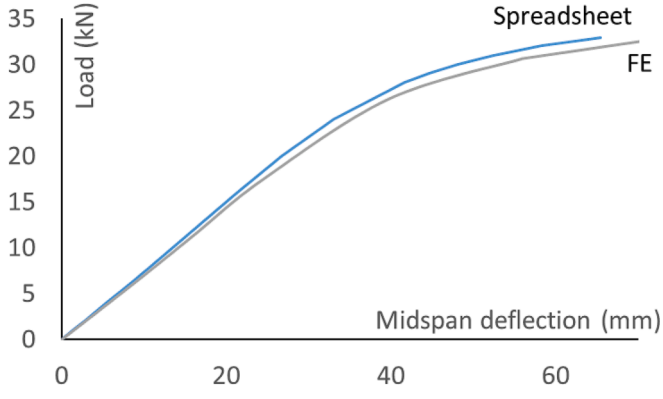

Fig. 31. Applied load versus midspan deflection for Tomasi et al. [23].

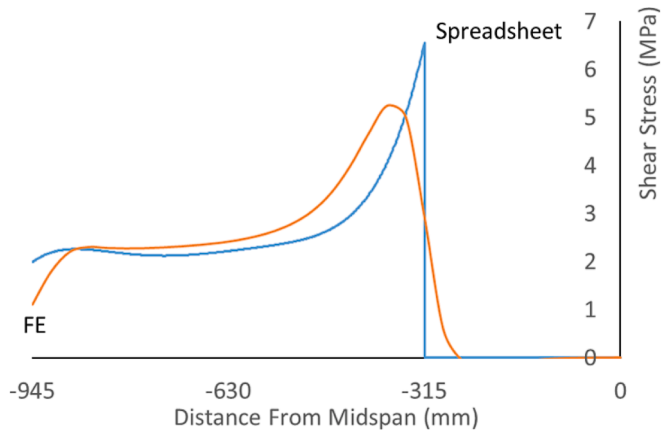

Fig. 32. Predicted peak longitudinal shear stresses at ultimate load, Tomasi et al. [23].

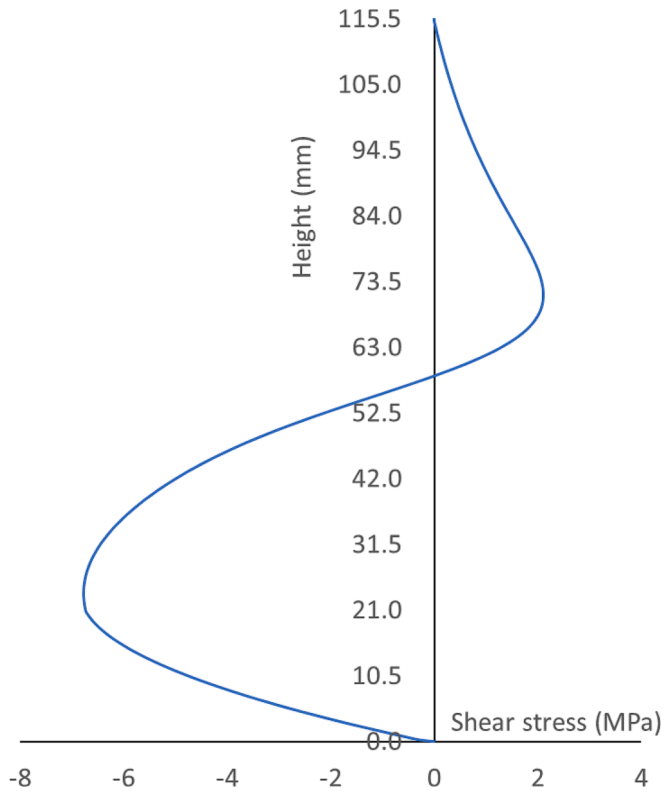

Fig. 33. Through-depth shear stress at load point at ultimate, Tomasi et al. [23].

between shear stress peaks, 60 mm is only 3.2% of the beam span, while the peak stress ratio is 1.32. Hence the assumption of shear-rigid timber in the spreadsheet leads to modest errors relative to the FE which employs finite shear moduli for the timber materials.

9.5. *Longitudinal shear bond stresses for Tomasi et al.*

Fig. 33 shows the through-depth distribution of shear stress at the section directly under the load point at ultimate. Compared to Fig. 17, where the shear stresses are all of the same sign, Fig. 33 shows a sign reversal along the height of the section. This reversal is a direct consequence of the post-peak fall-off of axial compressive stress in the Glos model after the peak point, bearing in mind the equilibrium relationship

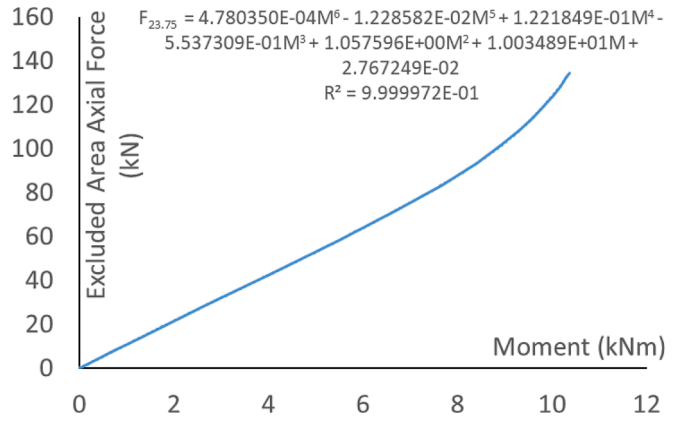

Fig. 34. $F_{ea}(M)$ plot for h = 23.75 mm.

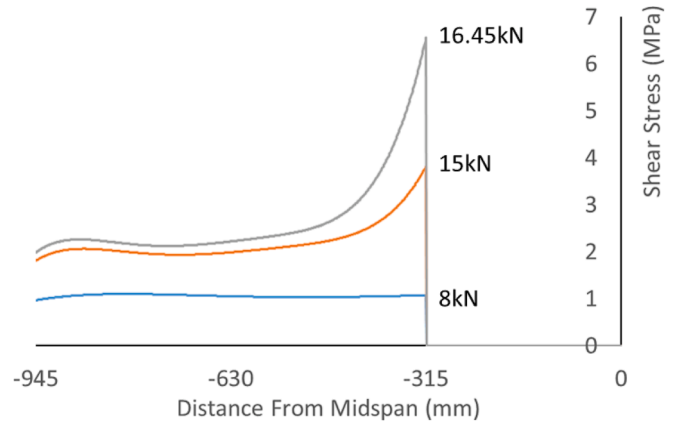

Fig. 35. Longitudinal shear stress profiles from spreadsheet, Tomasi et al. [23].

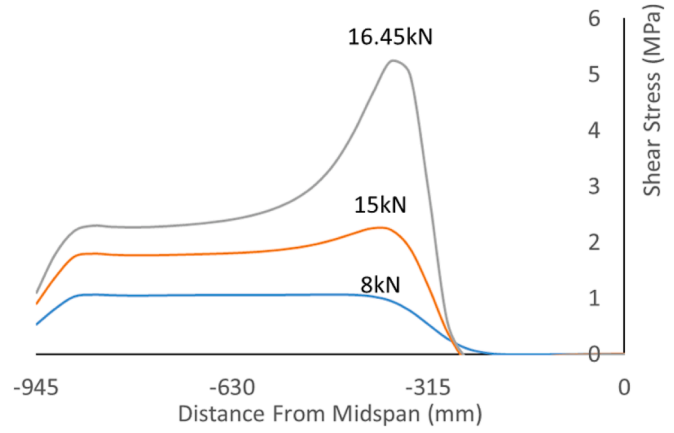

Fig. 36. Longitudinal shear stress from FE analysis, Tomasi et al. [23].

between the longitudinal shear stress and the derivative of the excluded area axial force (Fig. 6, Equation (9)). The axial force within the upper reaches of the section may change in opposition to the bending moment if the compressive strain goes beyond the peak point of the Glos strain–stress curve.

Fig. 34 shows the $F_{ea}(M)$ constitutive characteristic for h = 23.75 mm (where the peak shear stress occurs in Fig. 33), along with the regression equation and the R^2 value. This characteristic along with Equation (9) leads to the spreadsheet-predicted longitudinal shear stress profiles at

different load levels as shown in Fig. 35, with the corresponding FE predictions in Fig. 36. As previously, the trend persists of sharper and higher peaks on the spreadsheet curves relative to the more rounded and marginally lower peaks on the FE curves.

10. Conclusions

This paper presents a computational framework to study the nonlinear behaviours of hybrid timber joists which are ductile due to softening of the compression zone timber at high strains. The nonlinear constitutive behaviours of the timbers in compression can strongly influence the response of loaded hybrid glulam members in the approach to failure. In order to understand the associated load-displacement behaviours and stress redistributions, at the core of this framework are two section constitutive characteristics (SCCs), which express curvature and excluded area axial force both as functions of section moment, $\kappa(M)$ and $F_{ea}(M)$, and both (especially the latter) of which are novel features of the present study. When combined with longitudinal equilibrium and compatibility considerations, these SCCs permit rapid prediction of deflections and shear stresses well into the nonlinear regime.

Another novelty of the approach presented in this paper lies in its universality, owing to its programmability via spreadsheets. Hence the approach is useful in both design and research environments, and it produces high quality results well into the nonlinear regime in a highly time-efficient manner.

The computational framework is developed to predict deflections and longitudinal shear stresses along loaded hybrid timber joists, especially in the nonlinear regime when both these performance variables exhibit increasingly sharp rates of ascent with load. High order polynomial curve fitting is repeatedly utilised to describe the nonlinear constitutive behaviour at each stage of the analysis assuming zero slip and relaxation of finite shear deformations. The high order of the equations and high accuracy in the coefficients of the equations ensure high fidelity of the approach.

This twin SCC computational framework has been validated in two ways. One entails use of generalised load vs displacement data, namely local (M, κ) and global (P, δ) obtained from flexural loading tests on hybrid joists in two published studies. Now, the test data do not permit validation of spreadsheet-predicted shear bond stresses. Hence, the other way entails use of shear bond stress variations with load as predicted by FE analysis, itself validated using the above test data. Since the tests used multi-point loading, the FEA was subsequently used to also predict behaviour under Uniformly Distributed Loading of the same joists, from which excellent performance of the present computational approach has also been observed. The following key points arise from this study:

1. The twin SCCs which underpin this computational approach were double-checked by considering the section alternately as discretised and continuous.
2. Once the SCCs ($\kappa(M)$, $F_{ea}(M)$ and indeed $EI(M)$) have been output by the spreadsheet, they can be used repeatedly without any need to be recalculated from scratch each time. This considerably improves computational efficiency and time economy.
3. Specific features of spreadsheets are eminently suited to implementation of this approach, for example the *Goal Seek* function which expertly manoeuvres through nonlinear territory to track and identify relevant longitudinal equilibrium states.
4. Curve-fitting (regression analysis) is used not only to describe the material and section constitutive behaviours, but also to describe the spanwise behaviour (e.g. curvature profile) by application to the computed points at multiple stages of nonlinearity. The accuracy in coefficients of the curve-fitted polynomial equations influences the validity of the final results. It was observed that up to six-decimal places were needed particularly in the coefficients of the higher order terms of the polynomials, to enable reliable computation of key variables such as moments.
5. The present framework predicts ductility-influenced features (local $M(\kappa)$ nonlinearities, global $P(\delta)$ nonlinearities and shear stress redistributions) of load response that agree well with both test data and FE predictions throughout the nonlinear regime up to ultimate loads.
6. Under 4-point loading, there are pronounced nonlinear longitudinal and through-depth redistributions of shear bond stress near the span loads, with the peak shear stress occurring near the load points, due to the compression-zone timber ductility. However, the influence of material nonlinearity is not as pronounced under UDLs, which induce only gentle nonlinearities within the longitudinal shear stress profile near midspan, resulting in no change to the maximum shear stress locations (the supports) in proceeding from the linear to nonlinear regime.
7. A post-peak reduction in axial stress-strain behaviour leads to through-depth reversal of longitudinal shear stress in peak moment zones at high loads. This is because the shear stresses are related to the derivative of the excluded area axial force and so of the axial stress–strain characteristic.
8. For the examples considered here, under point loads the spreadsheet predicted peak shear stresses were 1.25–1.35 times the FE-predicted ones, with the two peaks occurring within 3.5% of the span away from each other. In future, stress concentration factors may be obtained in parametric studies on point load & member layouts. Under UDL, the spreadsheet-predicted nonlinear zone shear stresses are virtually identical to the FE-predicted ones.
9. This study shows that, provided the hybrid timber section comprises certain stacking sequences of different timber species, the load response can entail a pronounced semblance of ductile behaviour owing to compression zone nonlinearity, before failure occurs by fracture of the timber in the linear tensile zone.
10. The present approach, here applied to study of hybrid ductile glulam joists, can be adapted to other composite structural forms (e.g. timber concrete composites, with the added complexity of slip) which exhibit nonlinear behaviour, by curve-fitting the constitutive nonlinearities at the material and section levels, combined with equilibrium and compatibility requirements along the members for the loads of interest.

Declaration of Competing Interest

The authors declare that they have no known competing financial interests or personal relationships that could have appeared to influence the work reported in this paper.

Reference

[1] Harte AM, Baylor G, O'Ceallaigh C. Web geometry optimisation of novel latticed LVL-webbed timber I-joists. Structures 2023;47:748–759. 10.1016/j.istruc.2022.11.059.
[2] Dickson, Michael, and Dave Parker. Engineered Timber and Structural Form in Sustainable Design. Proceedings of the Institution of Civil Engineers. Construction Materials 168, no. 4 (2015): 161–172.
[3] Di Nino, S, A Gregori, and M Fragiacomo. Experimental and Numerical Investigations on Timber-Concrete Connections with Inclined Screws. Engineering Structures 209 (2020): 109993.
[4] Dias, A.M.P.G, A.R.D Martins, L.M.C Simões, P.M Providência, and A.A.M Andrade. Statistical Analysis of Timber–concrete Connections – Mechanical Properties. Computers & Structures 155 (2015): 67–84.
[5] Monteiro, Sandra R. S, Alfredo M. P. G Dias, and Sérgio M. R Lopes. Bi-Dimensional Numerical Modeling of Timber–concrete Slab-Type Structures. Materials and Structures 48, no. 10 (2014): 3391–3406.
[6] Mudie, J, W.M Sebastian, J Norman, and I.P Bond. Relative Influences of Cracking and Connection Yield on Transverse Distributions of Moments and Reactions in Timber-Concrete Composites. Engineering Structures 236 (2021): 112090.
[7] Loss, Cristiano, and Buick Davison. Innovative Composite Steel-Timber Floors with Prefabricated Modular Components. Engineering Structures 132 (2017): 695–713.

[8] Sebastian, W.M. Switch from Connection Ductility to Reinforcement Ductility with Curvature Reversal in Timber-Concrete Composites. Construction & Building Materials 229 (2019): 116886.
[9] Tazarv, Mostafa, Zachary Carnahan, and Nadim Wehbe. Glulam Timber Bridges for Local Roads. Engineering Structures 188 (2019): 11–23.
[10] Hu, Qibin, Ying Gao, Xinmiao Meng, and Yue Diao. Axial Compression of Steel–timber Composite Column Consisting of H-Shaped Steel and Glulam. Engineering Structures 216 (2020): 110561.
[11] Buchanan, Andrew H. Bending Strength of Lumber. Journal of Structural Engineering (New York, N.Y.) 116, no. 5 (1990): 1213–1229.
[12] Lacroix, Daniel, and Ghasan Doudak. Towards Enhancing the Post-Peak Performance of Glued-Laminated Timber Beams Using Multi-Directional Fibre Reinforced Polymers. Engineering Structures 215 (2020): 110680.
[13] Cepelka, Martin, and Kjell Arne Malo. Moment Resisting on-Site Splice of Large Glulam Elements by Use of Mechanically Coupled Long Threaded Rods. Engineering Structures 163 (2018): 347–357.
[14] Blank, Lukas, and Andrea Frangi. Design Model for the Bending Resistance of Fibre Reinforced Glulam. Engineering Structures 211 (2020): 110385.
[15] Lam, Frank, and Jung-Kwon Oh. Performance of Canadian Glulam Columns with New Laminae E Requirements. Engineering Structures 172 (2018): 85–93.
[16] Glos P, Denzler JK,and Linsenmann P. Strength and stiffness behaviour of beech laminations for high strength glulam. CIB-meeting thirty-seven. Edinburgh:2004.
[17] Ehrhart, Thomas, René Steiger, Pedro Palma, Ernst Gehri, and Andrea Frangi. Glulam Columns Made of European Beech Timber: Compressive Strength and Stiffness Parallel to the Grain, Buckling Resistance and Adaptation of the Effective-Length Method According to Eurocode 5. Materials and Structures 53, no. 4 (2020).
[18] Wang, Mingqian, Xiaobin Song, and Xianglin Gu. Three-Dimensional Combined Elastic-Plastic and Damage Model for Nonlinear Analysis of Wood. Journal of Structural Engineering (New York, N.Y.) 144, no. 8 (2018): 4018103.
[19] Lu, Weidong, Zhibin Ling, Qifan Geng, Weiqing Liu, Huifeng Yang, and Kong Yue. Study on Flexural Behaviour of Glulam Beams Reinforced by Near Surface Mounted (NSM) CFRP Laminates. Construction & Building Materials 91 (2015): 23–31.
[20] Sirumbal-Zapata, Luis F, Christian Málaga-Chuquitaype, and Ahmed Y Elghazouli. A Three-Dimensional Plasticity-Damage Constitutive Model for Timber Under Cyclic Loads. Computers & Structures 195 (2018): 47–63.
[21] Martins, C. Health Assessment of Glued Laminated Timber Elements. PhD thesis, University of Coimbra, Portugal, 2018.
[22] Shioya, Shinichi. Bending Behavior and Design Method for Hybrid Timber–steel Bar Glulam Beam subjected to Short-term Loading. Nihon Kenchiku Gakkai Kōzōkei Ronbunshū 84, no. 756 (2019): 247–256.
[23] Tomasi, Roberto, Maria Adelaide Parisi, and Maurizio Piazza. Ductile Design of Glued-Laminated Timber Beams. Practice Periodical on Structural Design and Construction 14, no. 3 (2009): 113–122.
[24] Ross C.T.F. Shear Stresses in Bending and Shear Deflections. In Mechanics of Solids, 1–1. Elsevier, 1999.
[25] Xavier, J.C. et al. A Comparison Between the Iosipescu and Off-Axis Shear Test Methods for the Characterization of Pinus Pinaster Ait. Composites. Part A, Applied science and manufacturing 35.7 (2004): 827–840.
[26] Crespo, Jorge et al. Comparative Analysis of the Elastic Constants Measured via Conventional, Ultrasound, and 3-D Digital Image Correlation Methods in Eucalyptus Globulus Labill. Bioresources 12.2 (2017): n. pag.
[27] BS EN 14080:2013: Timber Structures. Glued Laminated Timber and Glued Solid Timber. Requirements. British Standards Institute, 2014.
[28] Liu, Fenglu et al. Variations in Orthotropic Elastic Constants of Green Chinese Larch from Pith to Sapwood. Forests 10.5 (2019): 456.